CHALMERS
UNIVERSITY OF TECHNOLOGY

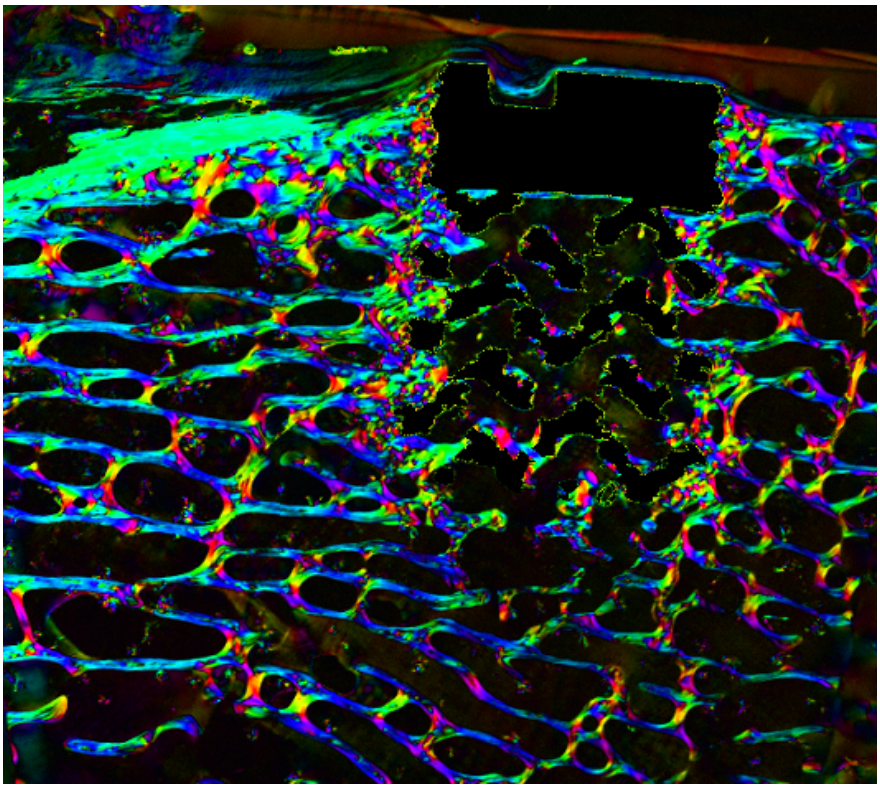

Study of bone anisotropy in porous metallic implants using birefringence and X-ray scattering imaging

Investigating the influence of geometry of porous metallic implants

Master's thesis in Biomedical Engineering

LUDVIG BJÖRK

DEPARTMENT OF PHYSICS
CHALMERS UNIVERSITY OF TECHNOLOGY
Gothenburg, Sweden 2023
www.chalmers.se

Master's thesis 2023

Study of bone anisotropy in porous metallic implants using birefringence and X-ray scattering imaging

Investigating the influence of geometry of porous metallic implants

LUDVIG BJÖRK

CHALMERS
UNIVERSITY OF TECHNOLOGY

Department of Physics
Division of Material physics
Liebi group
Chalmers University of Technology
Gothenburg, Sweden 2023

Study of bone anisotropy in porous metallic implants using birefringence and X-ray scattering imaging
Investigating the influence of geometry of porous metallic implants
Ludvig Björk

Supervisor: Adrian Rodriguez Palomo, Department of Physics, Chalmers University of Technology
Examiner: Marianne Liebi, Department of Physics, Chalmers University of Technology

Master's Thesis 2023
Department of Physics
Division of Material physics
Liebi Research Group
Chalmers University of Technology
SE-412 96 Gothenburg
Telephone +46 31 772 1000

Cover: The fast axis angle and the retardance of a metallic porous implant in bone.

Typeset in LaTeX
Gothenburg, Sweden 2023

Study of bone anisotropy in porous metallic implants using birefringence and X-ray scattering imaging
Ludvig Björk
Department of Material physics
Chalmers University of Technology

Abstract

Metallic implants are commonplace in orthopaedic surgery. Recent advances in manufacturing technology have made it possible to manufacture 3D printed porous implants. This allows for designs that are mechanically tailored to fit their environment. Bone growth in porous implants has been previously investigated, however this thesis studies the anisotropy of bone surrounding porous and non-porous metallic implants through imaging methods such as birefringence microscopy and small-angle X-ray scattering (SAXS).

Data from birefringence microscopy is corrected using Mueller calculus and the fast axis angle and retardance of bone is analysed. As the region of interest is too large for the microscope field of view, four images are stitched using the scale-invariant feature transform and random sample consensus algorithms. The birefringence data is validated through correlation with SAXS experiments. Additionally, 3D reconstruction of SAXS data is performed using real unrestricted spherical harmonic tensor tomography.

The validation of birefringence data indicates that the source of birefringence in bone is from collagen fibres. As a result, birefringence microscopy is used to show that fibres outside the area affected by implantation have a preferred orientation along the longitudinal axis and fibres inside of the porous implant have a preferred orientation that correlate with the geometry of the implant. Moreover, around the perimeter of the implant, bone growth is disordered as some fibres wrap around the outside of the implant, and some grow into pores. This shows that the geometry of the implant plays an important role in the anisotropy of bone, which can efficiently be studied using birefringence microscopy and SAXS.

Keywords: Porous implants, birefringence, collagen, SAXS.

Acknowledgements

I would like to acknowledge the Paul Scherrer Institute, Villigen, Switzerland for provision of synchrotron radiation beamtime at the beamline cSAXS of the SLS, the European Synchrotron Radiation Facility at the beamline ID15A, Kristina Stenborgs Stiftelse and the Wallenberg Wood Science Center (WWSC) for the financial support of the birefringence microscope as well as Anders Palmquist at Gothenburg University for providing the samples used in this thesis.

I extend my gratitude to my supervisor, Adrian Rodriguez Palomo, for supporting me wholeheartedly throughout this project. It would not have been possible to get this far without your input. A thanks to my supervisor Marianne Liebi for giving me the opportunity to learn so much during this project. I have truly enjoyed this time with Liebi research group and will always look back on it with fondness. Finally, I would like to thank everyone at the Division of Materials Physics for an awesome working environment, and for making my time there so great.

Ludvig Björk, Gothenburg, October 2022

List of Acronyms

Below is the list of acronyms that have been used throughout this thesis listed in alphabetical order:

CCD	Charge-coupled device
CoCr	Cobalt chromium
CSV	Comma-separated values
DoG	Difference-of-Gaussian
EM	Electromagnetic
FOV	Field of view
LED	Light-emitting diode
PEM	Photoelastic modulator
PMMA	Poly(methyl methacrylate)
RANSAC	Random sample consensus
RSM	Reciprocal space map
SAXS	Small Angle X-Ray Scattering
Ti	Titanium

Contents

List of Figures

1
Introduction

The use of metallic implants in surgical procedures dates as far back as 1565, but it was not until the early 19th century that the practice became successful, after the introduction of aseptic surgical procedures and metal alloys made specifically for human use. Before that, the implants often caused infections, due to the surgical procedure or the metal itself not being accepted into the body. During the 20th century cobalt chromium (CoCr) and titanium (Ti) became the most commonly used metals for orthopaedic surgery and prosthetics due to their biocompatibility, corrosion resistance and strength [3]. Today, the use of implants is most common as replacements of body parts such as knee or hip joints, but also as fracture fixation after trauma [4]. With an ageing population the demand for these surgeries is expected to increase, together with the need for revision surgeries. Repeated surgeries are mainly due to that implants undergo significant wear from mechanical stress and corrosion inside the body, resulting in that they have to be replaced. This has led to increased attention and research in the field of biomaterials to optimise the mechanical properties of the implants to improve its biocompatibility and lifespan. To assess the viability of implant designs they can be studied *in vivo* through animal trials. The bone around the implant is allowed to heal in the animal for some time and is then surgically removed together with its surrounding tissue. Through different imaging modalities, such as birefringence microscopy and X-ray scattering, the interaction between bone and implant can be investigated. Birefringence microscopy uses visible light to determine the optical properties of the material which makes it possible to study the anisotropy of bone in thin translucent samples. Small angle X-ray scattering, (SAXS), is an experimental technique that is sensitive to structures in the nanometer range which can also be used to study the anisotropy of bone. Birefringence and SAXS experiments utilises different physical effects and can therefore be seen as complementary to each other. Combining SAXS with scanning methods and tensor tomography it is possible to visualise both 2D and 3D samples [5]. In this thesis, birefringence microscopy and SAXS measurements will be used to study the interaction between bone and implant.

1.1 Aim

The aim of this thesis is to analyse the optical properties of collagen fibres in regenerated bone around CoCr and the Ti-alloy Ti6Al4V implants using birefringence microscopy. The samples contain both solid and porous geometries, with two different strut sizes. The process includes image acquisition, processing, stitching and

analysis. SAXS imaging, specifically scanning SAXS and Small angle scattering tensor tomography (SASTT), is used as a reference to the birefringence data. Scanning SAXS is used to identify the source of birefringence in bone while SASTT is used for additional analysis.

1.2 Limitations

Due to limited time in the beamlines, SAXS experiments will only be done for two samples, one for cortical bone and one for trabecular bone. These will be used for comparative analysis for birefringence microscopy and SAXS. The main imaging modality of the thesis is birefringence microscopy, and though scanning SAXS and SAXS tensor tomography is part of it, it will not be developed in more detail than necessary to perform the analysis.

2

Theory

This chapter introduces concepts used throughout the thesis. First, an overview of bone and its structure. Second, birefringence and birefringence microscopy is introduced as a method for imaging bone structure, followed by image processing. Finally, X-ray scattering, in the forms of SAXS and small-angle scattering tensor tomography (SASTT), wraps up the theory included in this work.

2.1 Bone structure

The skeletal system has many important functions in the body. Apart from providing support and protection to soft tissues, it stores minerals, such as calcium and phosphates, important for homeostasis. Some bones also contain red and yellow bone marrows which are important for the production of red blood cells and to store triglycerides. Bones are living tissue that undergo modelling and remodelling continuously influenced by, for example, load and stress but also hormones and mineral content [6].

2.1.1 Micro and macro structure

From a macroscopic perspective, bone can be loosely categorised as cortical (compact) bone and trabecular (spongy or cancellous) bone, seen in figure 2.1. Cortical bone is very dense and is commonly found as the outer shell of bones, and offers resistance to torsion and bending. Within cortical bone, cylindrical units known as osteons, containing Haversian and Volkmann's canals act as a transport system for blood vessels, nerves and lymphatic vessels, as seen in figure 2.1. Trabecular bone forms a scaffold inside the bone, creating space for blood vessels and bone marrow, and is resistant to impacts and load [7][8]. The architecture in trabecular bone is made from bone spicules that are usually around 0.2-0.4 mm thick, allowing for diffusion of nutrients without the need for osteons. Trabecular bone is more metabolically active than cortical bone, allowing for a more rapid modelling and re-modelling process. The main cell type found in mature bone is the osteocyte, a cell that maintains metabolism in the bone. It is formed by osteoblasts, a cell that produces mainly collagen, ultimately trapping itself in its extracellular matrix. Also present are osteoclasts, which are cells that break down the extracellular matrix, leading to a cycle of modelling and remodelling of bone. The extracellular matrix consists mainly of collagen type I and calcium phosphate salts.

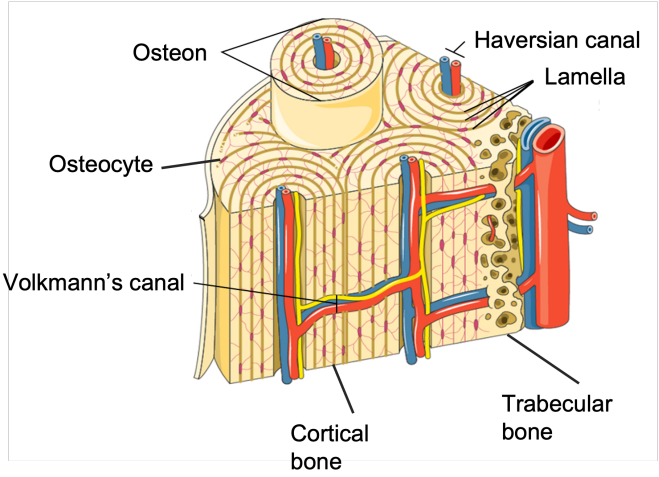

Figure 2.1: A schematic overview of the bone structure. The outer shell of the bone consists of cortical bone, which is oriented in a lamellar fashion and contains osteons, Haversian and Volkmann's canals to create space for nerves, blood and lymphatic vessels. The inside consists of trabecular bone that forms a scaffolding structure, which creates space for bone marrow and blood vessels. Adapted and reprinted under the Creative Commons License [1]

Collagen type I consists of amino acids bound in a triple helix formation known as tropocollagen. Tropocollagen is ~300 nm in length and assembles in parallel in groups of five to form microfibrils. As seen in figure 2.2, tropocollagen is separated by ~40 nm gaps in the longitudinal direction and has a periodicity of ~67 nm (D-period) to adjacent lines of tropocollagen [9].

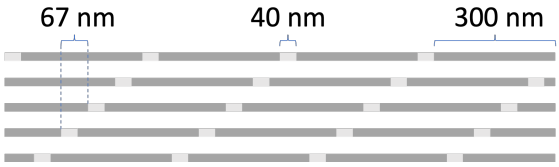

Figure 2.2: A schematic representation of the structure of bone microfibrils. ~300 nm long tropocollagen are separated by ~40 nm and offset by ~67 nm to adjacent lines.

The microfibrils are in turn also arranged in parallel into fibres whose dimensions are determined by the tissue that they form. In cortical bone, the fibres form highly organised lamellar structures, with each adjacent lamellae oriented in a different direction, similar to the structure of plywood [8]. While the collagen fibres have a high tensile strength, the c-axis of the calcium crystals within is parallel to that of the fibre, providing high compression strength [7].

2.1.2 Healing and metallic implants

In order to treat injured or missing bone, metallic implants may be used as substitution or support during the healing process. However, implantation itself causes

significant trauma to the bone in order to achieve the correct placement. The trauma causes activation of platelets in the blood, leading to the formation of clots as part of the coagulation process [10]. At the same time, the inflammation response is triggered, resulting in a complex interaction between signalling molecules, ultimately leading to the recruitment of mesenchymal stem cells. The mesenchymal stem cells migrate to the site of trauma and differentiate into the osteoblastic lineage. Bone formation occurs both at surrounding damaged bone, known as *distance osteogenesis*, and at the surface of the implant, known as *contact osteogenesis*. The interaction between metal and its surrounding tissue is dependent on the surface of the metal [11], and of the geometry of the implant [12]. If the implant material or surface topography does not allow for contact osteogenesis, it will not form a bond with the bone resulting in failed osseointegration. Initially, the mineralised collagen fibres are randomly oriented which is referred to as immature or woven bone. Over time, the woven bone is remodelled into lamellar bone. The mechanical properties of the implant are also of importance and according to the Mechanostat theory by Frost [13], bone responds to mechanical stress by adapting mass, geometry and strength. Young's modulus has been shown to be especially important and materials that are stiffer than bone may cause bone resorption around the implant [14]. On the other hand, the material must be able to withstand the forces exerted on the implant with sufficient strength and endurance. With the advancement of manufacturing techniques came the ability to manufacture more sophisticated geometries, and more recently, the ability to make previously impossible metal geometries through additive manufacturing. Without the need to cut away metal from a solid base the implants can be designed as scaffolds, allowing for implants that mimic the trabecular bone structures as well as the cortical bone structure [15].

2.2 Birefringence

When light waves propagates through a translucent medium the velocity of propagation is influenced by the dielectric and optical properties of the medium, such as refractive index. When the light waves impinges on the interface between mediums with different properties, the change in velocity leads to a change in direction, called refraction. If the medium is anisotropic, refraction is different depending on orientation. The polarisation state of the incident light wave then becomes a factor in the refraction process, as for example horizontally polarised light might not interact with the matter in the same way as vertically polarised light. The result is that the light waves are refracted in different directions. In *uniaxial* materials there is a single axis which governs the optical anisotropy, called the optical axis. Light propagating along this axis is called the *ordinary ray*, and the refractive index along this axis is n_o. Light propagating in other directions will be governed by another refractive index, n_{eo} and is separated into the *extraordinary ray*. This property of double refraction is called *birefringence* and is defined as the difference between the refractive index of the ordinary ray, n_o, and the extraordinary ray, n_{eo},

$$B = n_{eo} - n_o$$

The differences in refractive index means that there is a difference in velocity in the transmitted light. This will result in a difference in phase between the two outcoming rays. The phase shift between polarisation directions is called *retardance*, δ, and is related to birefringence through

$$\delta = T(n_{eo} - n_o)$$

where T is the thickness of the medium. The axis where the extraordinary ray propagates with the highest velocity through the medium is referred to as the fast axis, and slow axis for the contrary.

In collagen, this effect is due to a high degree of alignment of long bundles of fibres. If light impinges perpendicular to the fibre orientation, it will be refracted, while if it impinges parallel to the fibre orientation, it will not be refracted. This means that the optical axis, as well as the fast axis, in collagen fibres is along longitudinal direction of the fibre arrangement discussed previously. This effect is known as *form birefringence* [16]. In addition to form birefringence, the collagen molecules and the phosphate salts in the extracellular matrix exhibit a different kind of birefringence, namely *intrinsic birefringence*, and is due to the molecular and atomic structure [17]. This makes it important to locate the source of the signal in the birefringence microscope.

2.2.1 Polarisation states of light

Light propagating through birefringent materials, such as collagen, will have a different polarisation state. The change in polarisation is related to the structure of the material. An electromagnetic, (EM), wave can be described as a 2D vector

$$\mathbf{E} = \begin{bmatrix} E_x \\ E_y \end{bmatrix}$$

where E_x and E_y are the electric field x- and y-components of the EM wave. The polarisation state of light can be described using the Stokes parameters, defined as

$$\begin{aligned} S_0 =& |E_x|^2 + |E_y|^2 \\ S_1 =& |E_x|^2 - |E_y|^2 \\ S_2 =& 2 \cdot \mathbf{Re}(E_x E_y^*) \\ S_3 =& -2 \cdot \mathbf{Im}(E_x E_y^*) \end{aligned}$$

where S_0 is the total intensity, S_1 is the polarisation along the principal x- and y-axis, S_2 is the polarisation along the 45° shifted x'- and y'-axis and S_3 is the right or left hand circular polarisation component [18]. These components are often combined to what is called the Stokes vector, defined as

$$\mathbf{S} = [S_0 \quad S_1 \quad S_2 \quad S_2]^T$$

When the polarisation state of light changes as a result of some optical interaction it can be represented as the matrix transformation

$$\mathbf{S}_{out} = \mathbf{M}\mathbf{S}_{in}$$

Figure 2.3: A schematic overview of the optical path in the birefringence microscope.

where $\mathbf{M}$ is the 4×4 Mueller matrix [19]. If light passes through several optical elements that changes its polarisation, the Mueller matrix for the whole system becomes

$$\mathbf{M} = \mathbf{M}_N \mathbf{M}_{N-1} \cdots \mathbf{M}_2 \mathbf{M}_1$$

where the first element that light passes is 1 and the last N. Given two optical elements $\mathbf{M}_1$ and $\mathbf{M}_2$, one can extract $\mathbf{M}_2$ from

$$\mathbf{M}_2 = \mathbf{M}\mathbf{M}_1^{-1} \tag{2.1}$$

2.2.2 Birefringence microscopy

The present thesis uses the imaging system Exicor Birefringence MicroImager™ (Hinds Instruments, Inc., OR) for image acquisition as described by Freudenthal *et al.* [20]. The microscope features two polarisers and two photoelastic modulators (PEM), as seen in figure 2.3. Light is generated in a light-emitting diode (LED), travels along the optical path and is collected by a charge-coupled device (CCD). PEMs operate on the principle of photoelasticity, stress-induced birefringence, and modulates the polarisation state of the light propagating through the PEM. The modulation frequency for PEMs are tens of kHz which is too fast to register on the CCD. To overcome this issue, the microscope uses a stroboscopic light source as well as camera gating that together with two finely tuned PEMs only collects light that propagates through the PEMs within a certain range in the modulation. The intensity collected at the CCD is derived as

$$I(\delta_1, \delta_2) = M_{11} + C_{\delta 1} C_{\delta 2} M_{23} + C_{\delta 1} S_{\delta 2} M_{34} + S_{\delta 1} C_{\delta 2} M_{24} + S_{\delta 1} S_{\delta 2} M_{44} \tag{2.2}$$

where δ_n is the time dependent retardation of the PEM and M_{ij} is an element in the Mueller matrix. $C_{\delta n}$ and $S_{\delta n}$ are defined as

$$C_{\delta n} = \frac{\int_{t_{on}}^{t_{off}} \cos(A_n \cos(2\pi t + \phi_n) + \delta_{sn}}{t_{off} - t_{on}}$$
$$S_{\delta n} = \frac{\int_{t_{on}}^{t_{off}} \sin(A_n \cos(2\pi t + \phi_n) + \delta_{sn}}{t_{off} - t_{on}}$$

where A_n is the amplitude, ϕ_n is the phase constant, t_{off} and t_{on} are the pulse times and δ_{sn} is the static retardation of each PEM. For N measurements, equation (2.2)

can be expressed as

$$\mathbf{I} = \begin{bmatrix} I(\delta_{1A}, \delta_{2A}) \\ I(\delta_{1B}, \delta_{2B}) \\ \vdots \\ I(\delta_{1N}, \delta_{2N}) \end{bmatrix}$$

$$\mathbf{A} = \begin{bmatrix} 1 & C_{\delta 1A}C_{\delta 2A} & C_{\delta 1A}S_{\delta 2A} & S_{\delta 1A}C_{\delta 2A} & S_{\delta 1A}S_{\delta 2A} \\ 1 & C_{\delta 1B}C_{\delta 2B} & C_{\delta 1B}S_{\delta 2B} & S_{\delta 1B}C_{\delta 2B} & S_{\delta 1A}S_{\delta 2B} \\ \vdots & \vdots & \vdots & \vdots & \vdots \\ 1 & C_{\delta 1N}C_{\delta 2N} & C_{\delta 1N}S_{\delta 2N} & S_{\delta 1N}C_{\delta 2N} & S_{\delta 1N}S_{\delta 2N} \end{bmatrix}$$

$$\mathbf{M} = \begin{bmatrix} M_{11} & M_{23} & M_{34} & M_{24} & M_{44} \end{bmatrix}^T$$

Consequently, the elements in $\mathbf{M}$ can be extracted through the psuedo inversion of $\mathbf{A}$ as

$$\mathbf{M} = \mathbf{A}^{-1}\mathbf{I} \tag{2.3}$$

The angle of the fast axis, θ, and retardance, δ is then extracted through

$$\begin{aligned} \theta =& \text{sign}(M_{44})\frac{1}{2}\,\text{atan2}(M_{24}, M_{34}) \\ \delta =& \tan^{-1}(\sqrt{(\frac{M_{24}}{M_{44}})^2 + (\frac{M_{34}}{M_{44}})^2} \end{aligned}$$

where atan2 is the four-quadrant inverse tangent.

2.3 SIFT and RANSAC

The Scale-Invariant Feature Detection (SIFT) algorithm developed by Lowe [21], is a method for detecting features in an image. As the algorithm is implemented through a non-modified 3rd party software, it is only briefly discussed here for completeness. Following the original paper by Lowe, the SIFT algorithm can be described in 4 major steps:

1. **Scale-space extrema detection:**
   The original image is convolved with a difference-of-Gaussian (DoG) function,

   $$D(x, y, \sigma) = (G(x, y, k\sigma) - G(x, y, \sigma)) * I(x, y)$$

   where x and y are pixel coordinates, σ is the variance, k is a constant multiplicative factor and

   $$G = \frac{1}{2\pi\sigma^2}e^{-(x^2+y^2)/2\sigma^2}$$

   The DoG has a blurring effect on the images, and depending on k, they are considered to be in *scale-space* and the algorithm considers multiple values for k. Local extrema in the scale-space images are considered as keypoint candidates.

2. **Keypoint localization:**
   The keypoints are accurately localised by interpolation with the quadratic Taylor-expansion of $D(x, y, \sigma)$,

$$D(\mathbf{x}) = D + \frac{\partial D^T}{\partial \mathbf{x}}\mathbf{x} + \frac{1}{2}\mathbf{x}^T\frac{\partial^2 D}{\partial \mathbf{x}^2}\mathbf{x} \tag{2.4}$$

   where $\mathbf{x} = (x, y, \sigma)^T$ is the offset to the initial keypoint location. By taking the derivative of equation (2.4) with respect to $\mathbf{x}$ and setting it to zero, the location of the extrema is accurately localised. However, if the keypoints are located on an edge, the position may still be ambiguous. To improve stability these keypoints are removed through calculating the eigenvalues of the second-order hessian

$$\mathbf{H} = \begin{bmatrix} D_{xx} & D_{xy} \\ D_{yx} & D_{yy} \end{bmatrix}$$

   If the ratio $R = \mathrm{Tr}(\mathbf{H})^2/\det(\mathbf{H})$ is larger than 12.1 they keypoint is discarded. Additional keypoints that have low contrast to their neighbouring pixels are also discarded. What remains are stable, accurately localised keypoints, invariant to scale in the image.
3. **Orientation assignment:**
   The keypoints are localised in the original image smoothed with a Gaussian, $L(x, y\sigma) = G(x, y, \sigma) * I(x, y)$. At the scale of the keypoint,σ, the gradient magnitude, m, and orientation, θ, is calculated through pixel differences

$$\begin{aligned} m(x, y) =& \sqrt{(L(x+1, y) - L(x-1, y))^2 + (L(x, y+1) - L(x, y-1))^2} \\ \theta(x, y) =& \mathrm{atan2}(L(x, y+1) - L(x, y-1), L(x+1, y) - L(x-1, y)) \end{aligned}$$

   This is done at every pixel in a region around the keypoint and are used to create an orientation histogram with 36 bins, where samples are weighted by the gradient magnitude. The peaks in the histogram are the dominant orientations, and the highest peaks are attributed to the specific keypoint.
4. **Keypoint descriptor:**
   The keypoint is made from a 16×16 region around the keypoint, where an orientation histogram with 8 bins is calculated for each subregion. To ensure rotation invariance, the region is rotated relative to the keypoint orientation. The descriptor is a 128 element vector containing all the bins from all subregions, which is matched between images.

After the descriptors have been calculated for two images and the descriptors have been matched between the images, one of the images must be warped to align with the other one. Random sample consensus, (RANSAC), is a method of fitting a model to experimental data which is robust against outliers and gross errors [22]. In the present case, keypoints in one image is transformed through the 2D affine transform

$$\begin{bmatrix} \mathbf{y} \\ 1 \end{bmatrix} = \left[\begin{array}{cc|c} & \mathbf{A} & \mathbf{T} \\ 0 & 0 & 1 \end{array}\right] \begin{bmatrix} \mathbf{x} \\ 1 \end{bmatrix} \tag{2.5}$$

where $\mathbf{A}$ is a 2×2 matrix that describes rotation, shear and scale and $\mathbf{T}$ is a 2×1 vector that describes translation. This transform requires 3 points to satisfy the 6 free parameters in $\mathbf{A}$ and $\mathbf{T}$. With RANSAC, 3 points are randomly selected from all the keypoints from the image that is to be transformed, and used to calculate the inverse of (2.5). The estimated transform is then calculated on all the keypoints and the residual lengths between all corresponding keypoints are measured. The ratio of points that lie within a threshold i.e. inliers, to those that do not i.e. outliers, is referred to as inlier ratio, ε. The probability of selecting n outliers is $1-\varepsilon^n$. RANSAC is an iterative process, and for every iteration, k, the number of inliers is saved if it is greater than previous iterations, or discarded if it is less. The probability of selecting n outliers in k iterations is $(1-\varepsilon^n)^k$. Since the model most likely includes errors, a termination criterion is required. By establishing a threshold for the probability that the model is wrong, η, the termination criterion is defined as

$$k_{max} = \frac{\ln(\eta)}{\ln(1-\varepsilon^n)}.$$

2.4 X-ray scattering

X-rays are also EM radiation, but has a shorter wavelength and thus a higher energy than visible light. X-rays with energies above 5-10 keV are called *hard* X-rays and are widely used because of their high penetration depth. While it is common to study the absorption of X-rays, in for example medical radiology to image bone fractures, it is also possible to study the scattering of X-rays. When X-rays interact with atoms, the electrons oscillate with the flux of the EM wave, causing them to emit their own EM field, identical in phase and wavelength to incident X-rays. Many such elastic scattering events will interfere constructively to form a scattered wave if Bragg's law is fulfilled, stated as

$$n\lambda = 2d\sin(\phi) \tag{2.6}$$

where n is a positive integer, λ is the wavelength of the incident X-ray, d is the distance between scattering events, ϕ is the scattering angle. It is convenient to introduce a wave vector $\mathbf{k}$ to describe the propagation of the EM waves. As seen in figure 2.4, part of an incident X-ray is scattered as $\mathbf{k}_s$ at an angle of 2θ while part of the X-ray is transmitted without interaction as $\mathbf{k}_t$. The constructive interference occurs when the X-ray is scattered in planes separated by a distance d. The difference $\mathbf{k}_t - \mathbf{k}_s$ is defined as $\mathbf{q}$ and can be related to d through

$$|\mathbf{q}| = \frac{2\pi}{d} \tag{2.7}$$

By combining equations (2.6) and (2.7), constructive interference occurs at

$$|\mathbf{q}| = \frac{4\pi}{\lambda}\sin(\theta) \tag{2.8}$$

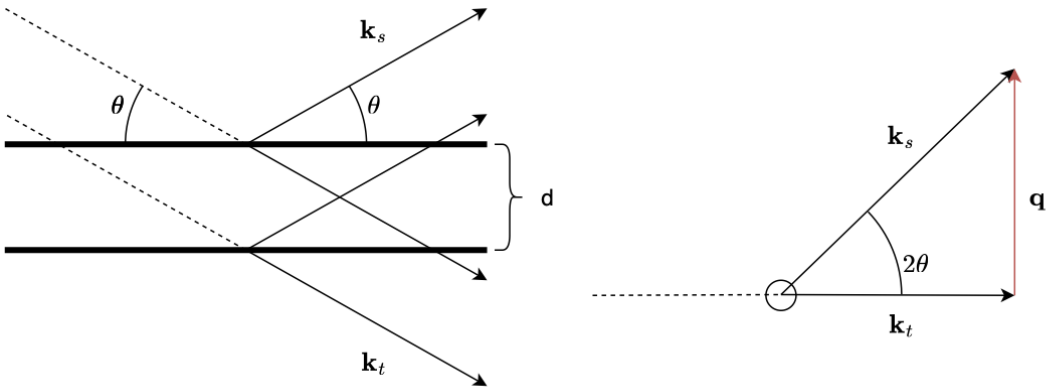

Figure 2.4: A schematic representation of the scattering process. Part of an incident X-ray (dashed) is scattered as $\mathbf{k}_s$ at an angle θ while the remaining part is transmitted as $\mathbf{k}_t$. Left: Planes of repeating structures with a separation of d that causes scattering. Right: An incident X-ray (dashed) being scattered from an outside point of view. The difference $\mathbf{k}_t - \mathbf{k}_s$ defines the vector $\mathbf{q}$.

2.4.1 Small angle X-ray scattering

In order to analyse repeating structures in the nanometer range the angle must be sufficiently small. In SAXS experiments the detector is usually placed meters away from the sample in order to resolve angles smaller than 0.1° [23]. The intensity of scattered X-rays is dependent on the amount of scattering events. The probability of X-rays interacting with electrons is low, making the difference in electron density between components in the sample the deciding factor for contrast [24]. Many times this leads to that the intensity of transmitted X-rays is much larger than that of scattered X-rays. For this reason transmitted X-rays are often blocked or measured separately from scattered X-rays. In addition to using $|\mathbf{q}|$, the azimuthal angle ϕ, of the scattered X-ray can be used to determine the orientation of the repeating structures in the sample, as seen in figure 2.5. Anisotropic structures produce anisotropic scattering patterns that can be used to retrieve information about the orientation and the anisotropy of such structures.

2.4.2 SAXS imaging

Scattering occurs within the volume of the sample that is illuminated by the X-ray beam. One method of analysing samples is to perform the measurement at several different locations. Usually the sample is moved on a motorised stage in a plane perpendicular to the incident X-ray beam and information about scattered X-rays is collected at each step. The desired parameter is extracted for each step and combined to an image, where the spatial resolution is determined by the size of the beam and step length of the motorised stage. This method is referred to as scanning SAXS but it is limited to the projection of structural information onto the 2D plane.

In order to get information about the 3D anisotropy, tomographic methods have been developed to obtain a 3D reconstruction of the reciprocal space map (RSM)

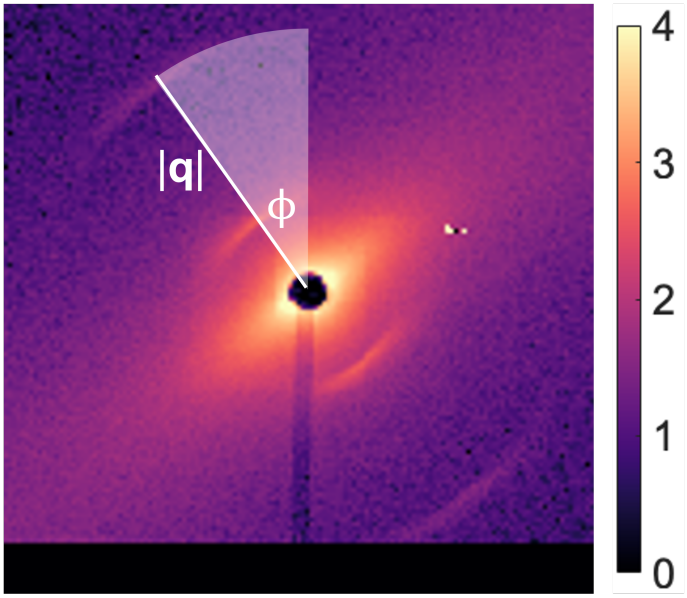

Figure 2.5: A detector image from a SAXS experiment. Repeating structures in the material causes scattering, which can be seen at $|\mathbf{q}|$ and azimuth angle ϕ.

In the case of X-ray absorption, a 2D projection is acquired from different angles, usually by rotating the sample. The projections are then used locate the volume element, i.e. voxel, in 3D space that is the cause of absorption and attributing a scalar to it. In the case of determining anisotropy however, it is necessary to attribute a tensor to each voxel. This requires an additional degree of freedom, which is introduce by rotating the sample around an additional axis. A method for SASTT was developed by Liebi *et al.* [5, 25], and recently further improved by Nielsen *et al.* [26]. The method utilises the fact that the image acquired at the detector is in reciprocal space. Assuming point symmetry around $q = 0$, spherical harmonics $\hat{Y}_m^l$ of even-order m and degree l can be used as a the basis functions to model the 2D RSM. The 2D data is used to reconstruct the 3D RSM and subsequently the tensor for each voxel.

3
Method

This section includes information about the experiment and process. It includes sample preparation, image processing, analysis and the SAXS experiment details.

3.1 Sample preparation

Thin slices, 35-40 µm thick, were prepared as previously described by Shah *et al.* [2]. In short, CoCr and Ti6Al4V implants were constructed in an interconnected open-pore scaffold through additive manufacturing using particles <100 µm in size, as seen in figure 3.1. The implants have a 2 mm solid top to match the layer of compact bone, while the 5mm open-pore scaffold is surrounded by trabecular bone. The implants were operated into the femur and tibia of 5 sheep and blocks containing the implants and surrounding bone were removed after 26 weeks. The blocks were embedded in plastic resin (LR White, London Resin Co. Ltd, UK), glued on to poly(methyl methacrylate), (PMMA), slides and ground to the above mentioned thickness. Additional sampled were prepared, as described by Palmquist *et al.* [15], using Ti6Al4V for both solid and open-pore samples, however the struts of the open-pore samples was larger than the ones from Shah *et al.* Samples from

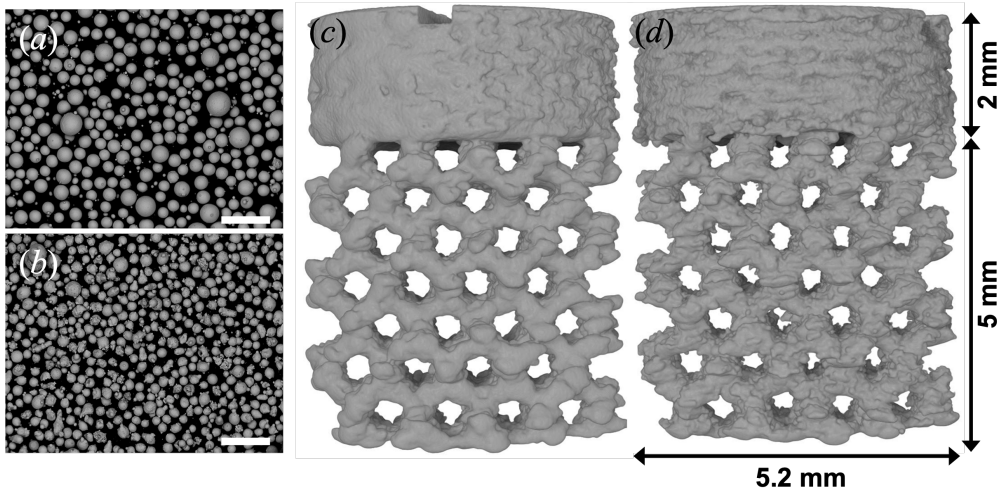

Figure 3.1: Scanning electron microscope images of Ti6Al4V (a) and CoCr (b) particles used for additive manufacturing. 3D rendering of micro-CT data showing the Ti6Al4V (c) and CoCr (d) implants. Modified with permission from Shah *et al.* [2]

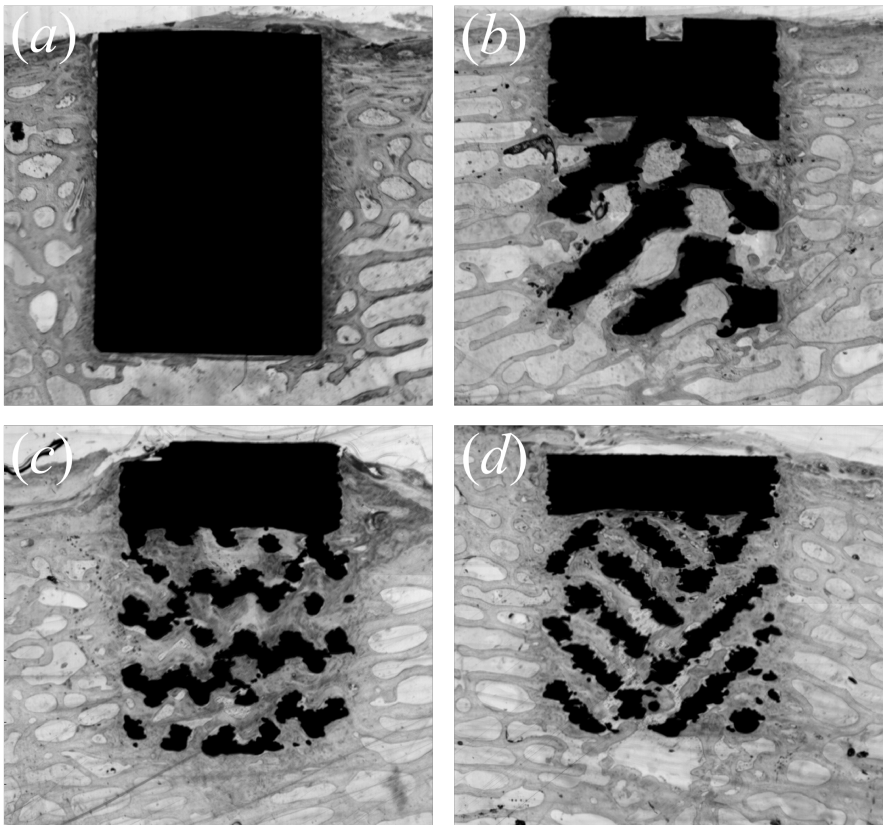

Figure 3.2: Samples containing implants of different geometries; (a) Solid Ti6Al4V, (b) porous Ti6Al4V with large struts, (c) porous Ti6Al4V with small struts, (d) porous CoCr with small struts.

each group are shown in figure 3.2 and an overview of all samples can be seen in appendix A.1.

3.2 Birefringence microscopy

The samples were investigated using the imaging system Exicor Birefringence MicroImager™ (Hinds Instruments, Inc., OR), technical details are found in Appendix A.2. The optical path of the microscope consists of a polariser and a PEM before entering the sample, followed by a PEM and a polariser and lastly impinging on a CCD detector. The optical path can be seen in figure 2.3 and detailed description of the microscope is given in section 2.2.2. Data from 41 samples containing trabecular bone were acquired with a magnification of 2x (Field of view 5.69×5.69 mm, pixel size 2.78 µm, resolution 5 µm). In addition, data from a sample containing trabecular bone was acquired with a magnification of 10x (Field of view 1.14×1.14 mm, pixel size 0.56 µm, resolution 2 µm). After the microscope had reached thermal equilibrium, the samples were placed in the microscope such that the flat solid top of the implant aligned with the top horizontal part of the camera view, as seen in figure 3.3. All the images were acquired using wavelengths of 475 nm and 655 nm. The resulting data was saved in the comma-separated values file format in three

files, one containing an image of the sample, one containing the calculated fast axis angle and one containing the calculated retardance.

3.2.1 Background correction

The samples are placed on PMMA slides which causes angle-specific retardation. To separate the optical effects of the slide, the empty part of the slide was measured. Assuming that the optical element is a linear retarder, the Mueller matrix is given as

$$\mathbf{M} = \begin{bmatrix} 1 & 0 & 0 & 0 \\ 0 & \cos^2(2\theta) + \sin^2(2\theta)\cos(\delta) & \cos(2\theta)\sin(2\theta)(1-\cos(\delta)) & \sin(2\theta)\sin(\delta) \\ 0 & \cos(2\theta)\sin(2\theta)(1-\cos(\delta)) & \cos^2(2\theta)\cos(\delta) + \sin^2(2\theta) & -\cos(2\theta)\sin(\delta) \\ 0 & -\sin(2\theta)\sin(\delta) & \cos(2\theta)\sin(\delta) & \cos(\delta) \end{bmatrix} \tag{3.1}$$

where δ is retardance and θ is the fast axis angle. The Mueller matrix of the sample was calculated using equations (3.1) and (2.1), with $\mathbf{M}_1$ being the Mueller matrix of the slide and $\mathbf{M}$ being the combined sample and slide data. To avoid local artefacts being transferred from the background measurement during the calculations, the centre of distribution in the retardance and the fast axis angle were used for δ_1 and θ_1 when constructing the Mueller matrix. The corrected angle of the fast axis, θ_c, and retardance, δ_c, was calculated using

$$\delta_c = \sqrt{(\frac{M_{3,4}}{M_{4,4}})^2 + (\frac{M_{2,4}}{M_{4,4}})^2}$$
$$\theta_c = -\frac{1}{2}\,\text{atan2}(M_{2,4}, M_{3,4})$$

where $M_{i,j}$ are elements in $\mathbf{M}_2$ and atan2 is the four-quadrant inverse tangent function. In order to evaluate the correction, a birefringent polymer film was measured on a PMMA slide. A background measurement was made on only the PMMA slide. As a reference, the polymeric film was also measured without the PMMA slide.

3.2.2 Image processing

Images were processed using MATLAB [27]. In order to remove artefacts and reduce noise, the images were masked using both retardance and intensity data. A retardance mask was created by removing values lower than a certain threshold and an intensity mask was created by removing values above a certain threshold. As the samples vary in thickness and transparency, no general thresholds could be set and were uniquely determined for each sample. In case of noticeable artefacts, e.g. cracks, a freehand mask was used to remove the area containing the artefact. The masks were then overlapped and applied to all datasets. The field of view (FOV) was increased by stitching 4 images, seen in figure 3.3, as described in section 2.3. The feature detection was made using VLSift from the VLFeat library in MATLAB [28]. The keypoints were matched and fitted using RANSAC with initial parameters $\eta = 0.01$ and $\varepsilon = 0.9$. The retardance and fast axis angle data were combined in a hue saturation value, (HSV), color scale, where the fast axis angle is the hue, and

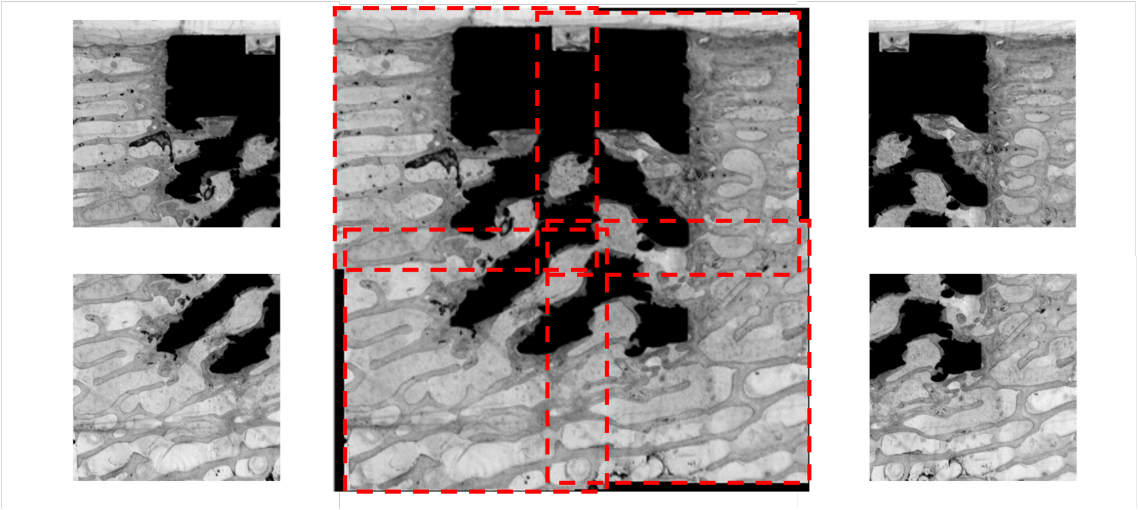

Figure 3.3: 4 images per sample were captured with the microscope and stitched together.

the retardance is the saturation, as seen in figure 3.4. The colour in the image represents the angle of the fast axis, which correlates to the angle in the colourwheel in 3.4(d). The brightness in the image is determined by the retardance, which means that areas with high retardance will appear bright, and areas with low retardance will appear dark.

3.2.3 Image analysis

To investigate the fast axis angle and retardance inside and outside of the porous implants, regions in the images were isolated and analysed. In order to extract the edges from the fast axis angle data, the DoG was calculated, as described in section 2.3. The standard deviations of the Gaussian filters used were 0.5 and 1.5 respectively and absolute values in the DoG less than 3 were removed. To prevent an edge to be detected as the angle smoothly changes from $-90°$ to $90°$, an additional copy of the data where angles were in the range of $0°$ to $180°$ was also used. The overlap in the images was used to mask the erroneous edges.

As an additional method of analysis, a map of the spatial distribution of fast axis angle was calculated. This was done by making a histogram with 32 bins for every column in the fast axis angle data. By arranging them consecutively, a surface was formed, where the x-axis was the fast axis angle distributions, the y-axis was the column number, and the z-axis was the counts in each bin of the histogram. This was used to analyse changes in fast axis angle with respect to distance from the implant.

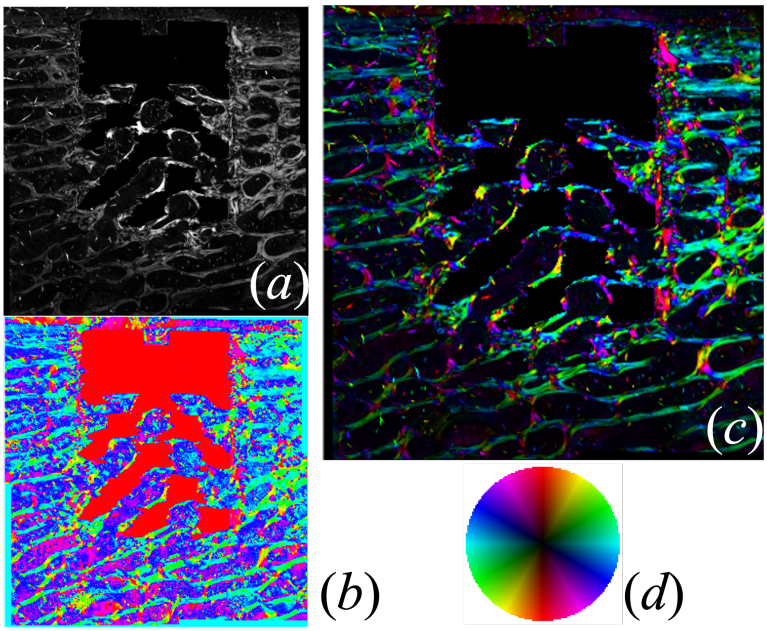

Figure 3.4: Figure depicting the combination of retardance data, (a), fast axis angle, (b), into a HSV color scale, (c). A colorwheel representing the fast axis angle is shown in (d).

3.3 Scanning SAXS

Two samples were used for scanning SAXS experiments at the cSAXS beamline, Swiss Light Source synchotron at Paul Scherrer Institute (PSI, Switzerland). A monochromatic X-ray beam was focused to a beam size of 27×9 µm, with a beam energy of 12.4 keV. The samples were placed on a motorised stage and raster scanned with a stepsize of 25×25 µm. The resulting FOV was 2.5×3 mm (101×121 points) for a trabecular bone sample and 2.12×2.25 mm (86×91 points) for a cortical bone sample. A 2 m flight tube was placed between the sample and the detector to minimise interference from air, and the transmission intensity was measured with a diode. The detector used was a Pilatus 2M (1475×1679 pixels, 172×172 µm^2/pixel). The distance between the sample and the detector was measured to 2.1729 m. Data processing was carried out using the "cSAXS scanning SAXS package" developed by the CXS group at PSI [29]. The 3rd order diffraction signal of collagen was extracted from $|\mathbf{q}|$ between 0.08 to 0.12 nm^{-1} from the overall scattering, as previously described by Georgiadis *et al.* [30].For the mineral contribution, $|\mathbf{q}|$ between 0.19 to 1.61 nm^{-1} was analysed.

3.4 SAXS tensor tomography

A total of 3 samples were used for the 3D reconstruction, one containing large strut implant from Palmquist *et al.* [15] and two containing small strut samples from Shah *et al.* [2] with one Ti6Al4V implant and one CoCr implant. The SASTT experiment was carried out at ID15A beamline at the European Synchrotron Radiation Facility

(ESRF, France). A 60 keV X-ray beam was focused to a size of 70×80 µm. The sample was raster scanned with a stepsize of 60×60 µm for each 2D projection. This was done at several different rotation angles (α) and tilt angles (β). For $\beta = 0$, the sample was rotated 0° to 180° and for $\beta \neq 0$ the sample was rotated 0° to 360°. The sample was tilted in intervals of 5° from 0° to 40°. This resulted in 259 projections for the solid and large open-pore samples, 258 projections for the CoCr sample and 245 for the small open-pore Ti6Al4V sample. For the reconstruction, $|\mathbf{q}|$ between 0.65 to 0.70 nm^{-1}, corresponding to the mineral contribution, was used.

4

Results and discussion

This chapter shows the results from the background correction and birefringence data validation, followed by analysis of bone anisotropy around metallic implants.

4.1 Birefringence background correction

In order to determine the optical properties of the sample, the influence of the PMMA slide was corrected using Mueller calculus. The effects of background correction on the fast axis angle is shown in figure 4.1. The uncorrected data, figure 4.1(a), shows a uniform background, caused by the anisotropy of PMMA. In figures 4.1(b)-(c), there appears to be less uniformity in the background, compared to the original data. As seen in figure 4.1(d)-(f), the fast axis angle in all datasets shows a sharp peak centred around $11 \pm 0.5°$, which corresponds to the fast axis angle of the polymer film. The anisotropy of PMMA results in a peak around $4 \pm 0.5°$, marked

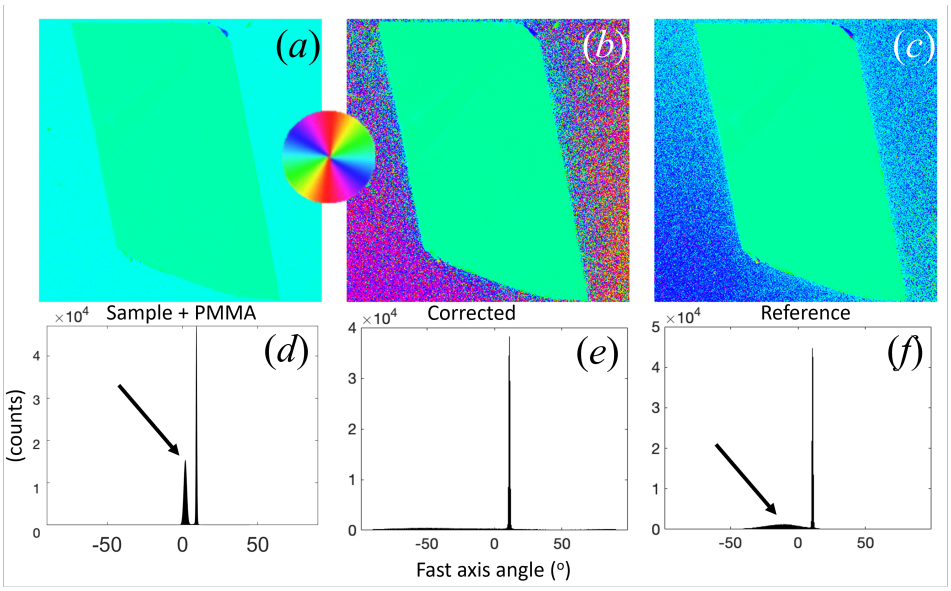

Figure 4.1: Fast axis angle of the uncorrected data, (a), and the corrected data, (b) of polymer film on a PMMA slide. Reference data of polymer film without the PMMA slide is shown in (c). Distribution of angles is shown in (d),(e) and (f) respectively, where sharp peaks corresponding to the polymeric film are seen at $11 \pm 0.5°$. The arrow in (d) shows the peak caused by the PMMA slide. The arrow in (f) shows the peak caused by the background in the reference data.

by an arrow in 4.1(d). In 4.1(e) there is no sharp peak from the fast axis angle of the PMMA, indicating that the background correction is working as intended. Interestingly, the background distribution in the reference data shows a more narrow distribution of angles centred around $-10 \pm 0.5°$, marked with an arrow in 4.1(f). This is most likely due to that the Mueller matrix of the background includes more of the optical path than the PMMA slide, such as the microscope carriage and lenses, which is suppressed in the correction. It should be noted that the sample was remounted when removing the PMMA slide, so even though peaks corresponding to the polymer film are at similar angles, it is difficult to separate the effects of the correction to that of slightly rotating the sample. By looking at figure 4.1(b)-(c), there is no significant difference in rotation of the sample between the corrected data and reference data. Another source of error comes from the distribution in fast axis angle from the background measurement. When the centroid is selected, the error introduced depends on the distribution width. However, since the distribution varied across the PMMA slide and did not appear to contribute above the resolution of the microscope, it was not further investigated.

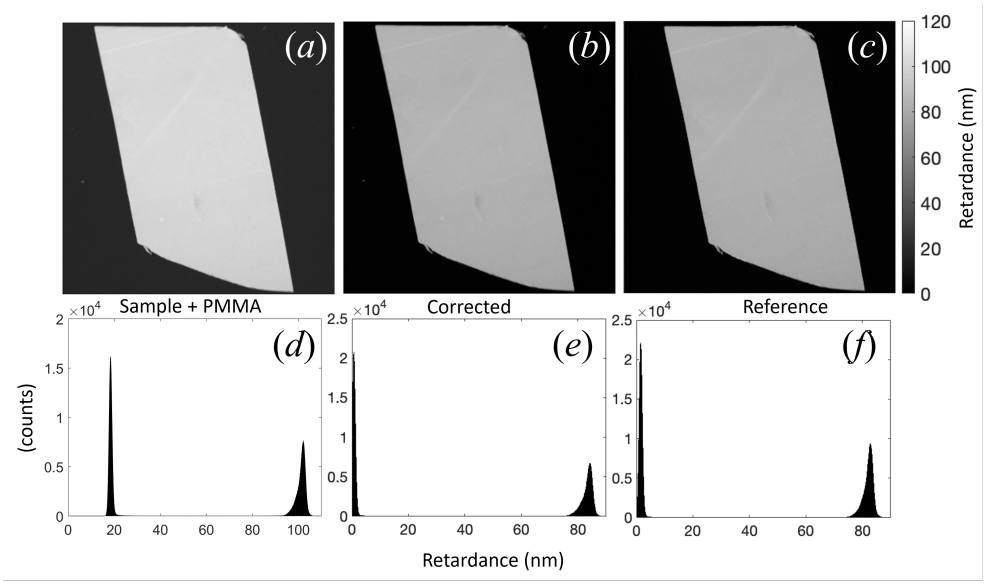

Figure 4.2: Retardance of the uncorrected data, (a), and corrected data, (b), of polymer film on a PMMA slide. Reference data of the polymer film without the PMMA slide is shown in (c). Distribution of retardance is shown in (d),(e) and (f) respectively.

Looking at figure 4.2, the retardance of the uncorrected data is higher than both the corrected data and the reference data. In 4.2(d), data containing only PMMA has a retardance centred around 18 nm, and the retardance of the PMMA and the polymeric film combined has a retardance centred around 102 nm. The effect of the data correction can be seen in figure 4.2(d)-(f), where the retardance of the polymeric film is seen as peaks centred at 84 nm and 83 nm for the corrected and reference data respectively. In the lower regions of the distributions, the retardance of the background can also be seen as a peak. In the corrected data, the retardance of the background is closer to 0 than in the reference data. As with the fast axis

angle data, this might be the effect of interference in the optical path in its entirety not being corrected for the reference data.

These results show that the optical properties of the sample can be extracted through Mueller calculus and that the extracted data corresponds to the reference data. This process is necessary for analysing the sample characteristics. Since it is not possible to measure the polarisation state of light at the interface between the PMMA slide and the sample, the data acquired by the microscope can not be used directly to draw conclusions about the sample. If measuring the combined effect of several optical elements, it would not be possible to locate where in the optical path the change of polarisation occurs. As an additional point, the result in this particular example illuminates how the background influences the experiment in different ways for the fast axis angle and the retardance data. The fast axis angle data does not suffer as much interference as the retardance data does. This is most likely due to the fact that the fast axis angle of the PMMA and the polymeric plastic are, in this case, somewhat aligned, making the retardance interference appear almost additive. As mentioned previously, that is not the case and Mueller calculus is necessary to properly correct for optical elements in the path.

4.2 Birefringence data validation through SAXS

Even though the optical properties of bone can be studied using birefringence microscopy, the structural component that is the cause of birefringence can not be determined solely through the acquired data. To find the source of birefringence, a SAXS experiment was carried out. A comparison between the data from measuring cortical bone with both scanning SAXS and birefringence microscopy is seen in figure 4.3. In the SAXS HSV images, the saturation and value components are the symmetric and asymmetric intensities, while hue is determined by angle, as represented by 4.3(e). Highly oriented materials appear as colourful, while low orientation appears as less colourful. The brightness is determined by scattering intensity. For collagen, the orientation of asymmetric intensity as well as symmetric intensity in the SAXS data seen in corresponds very well to the fast axis angle acquired with the birefringence microscope, seen in 4.3(a)-(b). Additionally, the dark spots in the SAXS data appear in similar places as dark spots in the birefringence data, which represents low retardance. Furthermore, to ensure that there is not an erroneous shift in angle from processing the birefringence data, the orientation of asymmetric and symmetric intensity from the mineral contribution was also compared to birefringence data. Seen in figure 4.3(c)-(d) is the SAXS data compared to birefringence data where the colourwheel has been rotated 90°. The dark spots with low retardance in the birefringence data is no longer matched with dark spots in the SAXS data. Since SAXS data is gathered from scattering events within a volume, one of the parameters is beam size. There is no direct correlation between the symmetric intensity and retardance, since retardance is not influenced by the surface area of the illuminated volume. For dark spots in the SAXS images there are few scattering events, and if this correlates with low retardance it indicates that there is not much collagen. These results indicate that the largest contribution to the birefringence

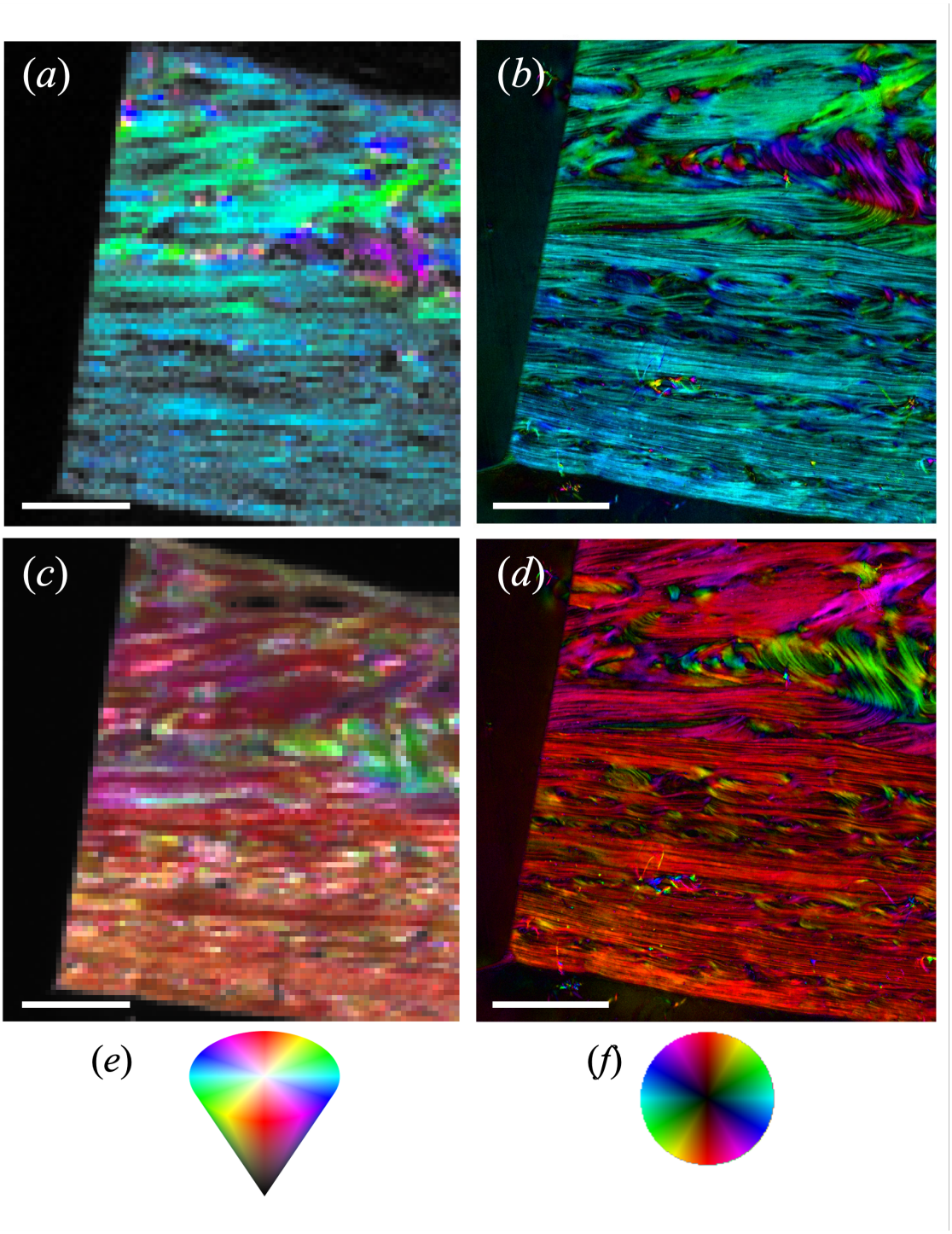

Figure 4.3: Comparison of experimental data from cortical bone. Orientation and intensity generated from scattering in collagen, (a) and birefringence data, (b). Orientation and intensity generated from scattering in mineral is shown in (c). Birefringence data that has a shifted colorwheel is shown in (d). The colorwheel used in (a) and (c) is shown in (e) and the colorwheel used in (b) is shown in (f). The colormap used in (d) is (f) rotated by 90° to match the orientation of mineral data.

signal is the birefringence of the collagen fibres but it is known that the staining used in the samples, toluidine blue, alters the birefringence when used with collagen [31]. Comparing measurements done at wavelengths 475 nm and 655 nm reveals no significant difference in neither retardance nor fast axis angle, indicating that the absorption of the stain does not significantly affect the birefringence. This further indicates that the data acquired in the birefringence microscope is due to the birefringence of collagen fibres, which means that birefringence microscopy can be used to study the anisotropy of collagen fibres. This is highly beneficial given the low complexity of birefringence microscopy compared to SAXS experiments. Another benefit is the possibility of easily expanding the number of samples, which is limited in SAXS due to time constraints.

4.3 Effects of implant geometry

The trabecular structure in the femur is adapted to distribute load and is typically oriented in the longitudinal direction of the bone [32]. However, by introducing an implant, the longitudinal direction is obstructed, blocking bone growth. To see how this affected fibre orientation, regions both outside and inside of the porous implants were studied through birefringence microscopy and X-ray scattering.

4.3.1 Collagen orientation inside porous implants

As seen in figure 4.4, collagen fibres exhibit different orientations in the regions inside and outside the porous implant, represented by white boxes in 4.4(a). In figure 4.4(b), the distributions in angles are marked with lines corresponding to the colormap of the HSV image in 4.4(a), where they are also indicated with arrows. Inside of the sample, collagen fibre orientation have two major angles of alignment, which seem to correspond to the geometry of the implant. Referring to the full set of measurements in appendix A.3, this effect is more pronounced in the samples with small struts. As previously reported, bone-implant contact is higher for Ti6Al4V than for CoCr [2], but the change in orientation is similar in both materials. This may indicate that the alignment is not necessarily only bound to the struts in the implant, but that the pores in the implants work as a guide. This could also explain why this effect is less pronounced in samples with large struts, where some experiments show a more random distribution with only one distinct peak inside the implant. It can also be seen that there was no clear alignment in the region outside the implant for this particular sample, but it does not appear to be the deciding factor for alignment inside of the porous implant. The impact of pore size has been previously studied, but consensus around the optimal size or shape is yet to be defined [33, 34]. It is not clear whether the difference between large and small struts is a consequence of a larger space between the struts or other factors such the rotation of the implant, as there are only 6 samples.

The distribution of retardance is shown in figure 4.4(c). In the region outside the implant, retardance distribution of collagen is seen as a hump around 25 nm, with a peak caused by the background near 0. As a trend, retardance had a wider dis-

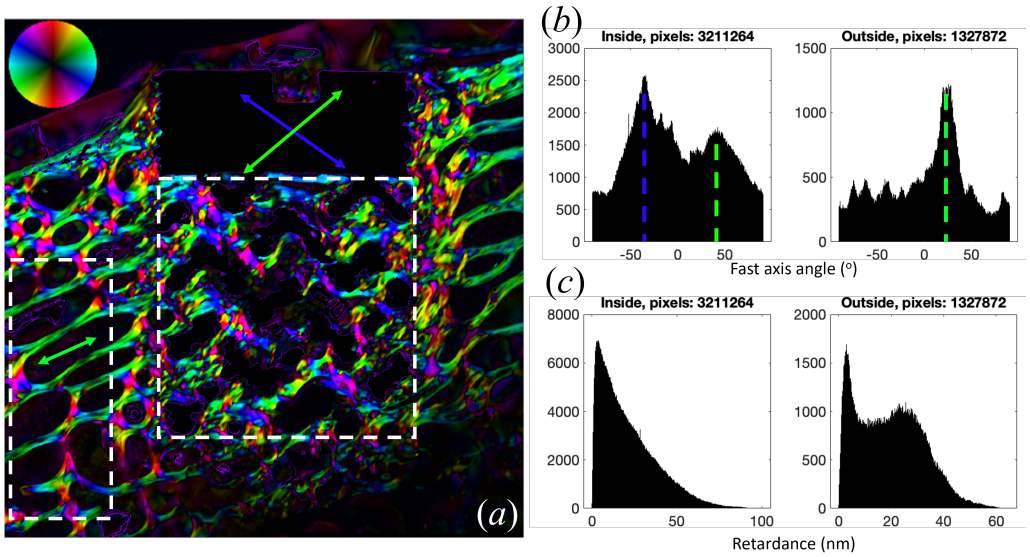

Figure 4.4: (a): An HSV image of a small strut porous implant where regions of interest are marked with white rectangles and the major angles are marked with arrows, with colour corresponding to the angle. (b): The distribution of angles in regions inside and outside the porous implant where major angles are marked with colour corresponding to the angle. (c): The distribution of retardance in regions inside and outside the porous implant.

tribution inside of the implant, without a clear centroid. As discussed in section 2.2, the measured retardance depends on the out-of-plane orientation of the optical axis of collagen, fibre density and sample thickness. The fact that spots with higher retardance is found inside the implant indicates that some of these parameters have changed, with the most likely being sample thickness. Metal is much harder than bone, so the grinding process most likely led to slightly thicker collagen within the sample. Additionally, since the first step in bone formation is in the form of woven bone, which is less birefringent than mature bone, fibre density could together with out-of-plane orientation of the optical axis explain the appearance of the distribution curve.

4.3.2 Collagen orientation at the implant perimeter

Around the perimeter of the implant, collagen orientation exhibits significant change in orientation. The fast axis angle in the perimeter of a solid implant can be seen in figure 4.5(a), where data containing low retardance and high transmission have been removed. In order to analyse rapid changes in orientation, the DoG of the angle data was calculated, as describe in 2.3 and seen in 4.5(d). The resulting image only contains the edges of parallel fibre bundles, and the number of pixels in each column is shown below the image. Closer to the implant, the number of pixels increases, meaning that there are more edges and thus a more rapid change in fibre alignment. Looking at the porous implants, seen in figures 4.5(b)-(c), where the implant perimeter is marked with a dark line, the trend is similar, but the disordered region

extends into the pores.

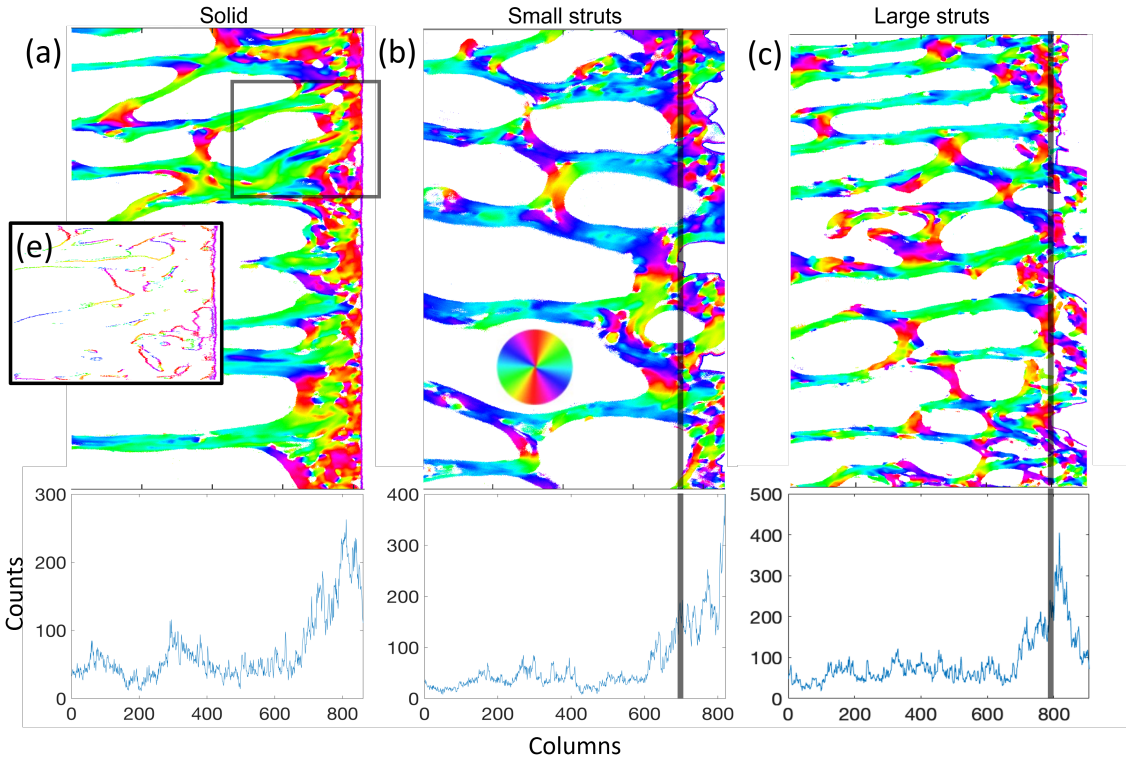

Figure 4.5: Fast axis angle data from collagen at the perimeter of a solid, (a), small strut, (b), and large strut, (c), sample with the implant located to the right. Part of the DoG image is shown in (e) where only the edges remain. Below each image, the number of pixels in each column of the DoG image is shown. In (b) and (c) the implant perimeter is indicated by a dark band in both the image and the plot.

As an additional imaging technique, SASTT was utilized to investigate mineralised collagen orientation. Reconstructions of the 3D RSM of the mineral particles in mineralised collagen around porous implants can be seen in 4.6, where tensor orientations and magnitudes are visualised flowlines. In 4.6(a), the implant is oriented similarly to the birefringence images, and orientation of collagen show similar behaviour. The degree of orientation is larger in the region outside of the implant and flowlines are aligned longitudinal to the bone. A darker band with more erratic behaviour in the flowlines is located along the perimeter of the implant with the same characteristics as the disordered region found analysed above. An isolated section along the vertical axis is seen from a top-down view in 4.6(b). Here, flowlines indicate that collagen fibres align partly into pores, and partly around the implant. The same trend is seen in the two small strut samples, as seen in figures 4.6(c)-(d). This correlates well to the measurements done with the birefringence microscope, as retardance is lower in this region and that fast axis angle changes rapidly. If the optical axis is close to parallel to the beam path of the microscope, small deviations cause large changes in fast axis angle, as this is the projection on to the 2D plane.

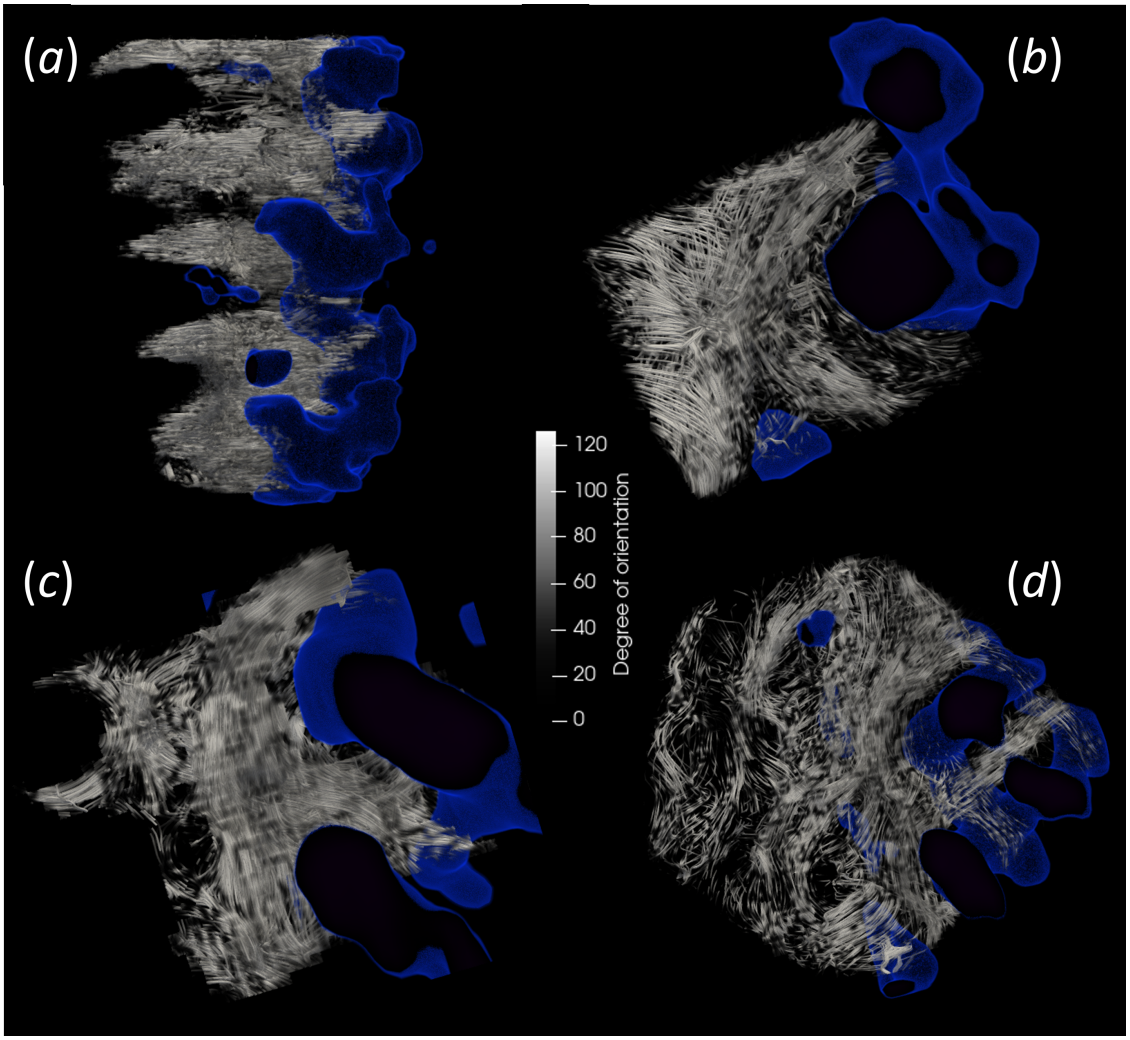

Figure 4.6: SASTT reconstruction of collagen fibre orientation. A side view from a large strut implant sample is shown in (a), and a top-view of the same sample is shown in (b). Small strut samples made from CoCr and Ti are shown in (c) and (d) respectively.

In the top-down view, artefacts from the large voxels appear as sharp cuts near the edges, and as a banded pattern in the flowlines.

By combining the two methods, it can be seen that the rapid change in fibre alignment around the perimeter of the implant is most likely due to that fibres tend to wrap around the implant as well as go into the pores. It is not clear whether it is a consequence of implant geometry or of the healing process. In the first step of implantation, a hole was drilled in the same size as the implant, from which distance osteogenesis occurs. The fact that trabecular structures are seen crossing the implant perimeter in both porous implants, indicates that the bone is fully healed and may be an indication that the fibre alignment is not completely due to healing. In addition, as discussed above, bone remodelling is adapted by mechanical forces. Since these implants do not have any external loading, the mechanical stress is from

loading in the longitudinal direction, as the sheep walks. Fibre alignment into the pores could be adaptation to this force, as bone growth attempts to strengthen the bone in the longitudinal direction. Fibres wrapping around the implant, however, would be an adaptation to torque applied to the implant. It is possible that this is a mechanism for stabilising the implant in the bone.

5

Conclusion

The aim of this project was to analyse the anisotropy of collagen near porous metallic implants with birefringence and X-ray scattering imaging. Solid, large and small strut samples were acquired from previous studies and the orientation of collagen fibres were analysed with birefringence microscopy and SASTT.

Data from the birefringence microscope was expanded to increase the FOV using SIFT and RANSAC, and Mueller calculus was utilised to reduce the optical interference from the PMMA slide, increasing the contrast of the sample. In order to determine the source of birefringence, SAXS was utilised to correlate scattering from the collagen fibres to the data from the birefringence microscope. In addition, birefringence data was used to show that scattering from the phosphate minerals in bone is not the major contributor to the measured signal. The correlation with X-ray scattering validated the data gathered through birefringence microscopy in a very valuable way, since it allowed for insights into collagen that could not be acquired through birefringence alone. On the other hand, the amount of samples studied with birefringence microscopy would not have been a feasible endeavour with SAXS experiments.

Analysing the samples, while collagen outside of the porous implant has a tendency to align longitudinal to the bone, alignment inside of the porous implant is influenced by the geometry of the implant. This was more pronounced in the small struts samples, possibly due to the limited space compared to the large struts samples. It was also shown that all samples had a region at the perimeter of the implant where the collagen fibres orientation changed. In the birefringence microscope, this was seen as disordered region with rapid changes in both retardance and fast axis angle. SASTT revealed that the fibres aligned around the outside of the implant, and if present, into pores. This region did not specifically follow the cylindrical cut from the drill, indicating that the trauma may not necessarily be the cause of the interrupted alignment. These conclusion was drawn from both birefringence data and X-ray scattering experiments, signifying the benefit of combining the two methods.

The geometry of metallic implants influence the orientation of collagen fibres, both inside the pores and at the perimetere of the implant. Collagen fibres tends to wrap around the outside of implant and follow the orientation of the struts. For future research, it would be of interest to examine geometries that promote growth in the same orientation as the surrounding trabecular structure, by for example

having pores only longitudinal to the bone. Another feature to examine could be the perimeter geometry. If the fibres wrapping around the sample do protect from torque, having a square implant might reveal this. In addition, a control group where holes have been drilled but without an inserted implant would help determine the impact of healing around the cut line.

Bibliography

[1] S. M. A. by Servier, "Osteon." [Online]. Available: https://smart.servier.com/smart_image/bone-structure-2/

[2] F. A. Shah, O. Omar, F. Suska, A. Snis, A. Matic, L. Emanuelsson, B. Norlindh, J. Lausmaa, P. Thomsen, and A. Palmquist, "Long-term osseointegration of 3d printed CoCr constructs with an interconnected open-pore architecture prepared by electron beam melting," *Acta Biomaterialia*, vol. 36, pp. 296–309, May 2016. [Online]. Available: https://doi.org/10.1016/j.actbio.2016.03.033

[3] A. Balamurugan, S. Rajeswari, G. Balossier, A. Rebelo, and J. Ferreira, "Corrosion aspects of metallic implants — an overview," *Materials and Corrosion*, vol. 59, pp. 855 – 869, 11 2008.

[4] A. Pandey, A. Awasthi, and K. K. Saxena, "Metallic implants with properties and latest production techniques: a review," *Advances in Materials and Processing Technologies*, vol. 6, no. 2, pp. 405–440, Mar. 2020. [Online]. Available: https://doi.org/10.1080/2374068x.2020.1731236

[5] M. Liebi, M. Georgiadis, A. Menzel, P. Schneider, J. Kohlbrecher, O. Bunk, and M. Guizar-Sicairos, "Nanostructure surveys of macroscopic specimens by small-angle scattering tensor tomography," *Nature*, vol. 527, no. 7578, pp. 349–352, Nov. 2015. [Online]. Available: https://doi.org/10.1038/nature16056

[6] G. Tortora and B. Derrickson, *Introduction to the Human Body*. Wiley, 2011.

[7] F. Safadi, M. Barbe, S. Abdelmagid, M. Rico, R. Aswad, J. Litvin, and S. Popoff, *Bone Structure, Development and Bone Biology: Bone Pathology*, 12 2009, pp. 1–50.

[8] J. A. Buckwalter, M. J. Glimcher, R. R. Cooper, and R. R. Recker, "Bone biology. i: Structure, blood supply, cells, matrix, and mineralization." *Instructional course lectures*, vol. 45, pp. 371–86, 1996.

[9] S. R. Stock, "The mineral–collagen interface in bone," *Calcified Tissue International*, vol. 97, no. 3, pp. 262–280, Apr. 2015. [Online]. Available: https://doi.org/10.1007/s00223-015-9984-6

[10] P. R. Kuzyk and E. H. Schemitsch, "The basic science of peri-implant bone healing," *Indian J. Orthop.*, vol. 45, no. 2, pp. 108–115, Mar. 2011.

[11] I. Milošev, V. Levašič, S. Kovač, T. Sillat, S. Virtanen, V.-M. Tiainen, and R. Trebše, "Metals for joint replacement," in *Joint*

Replacement Technology. Elsevier, 2021, pp. 65–122. [Online]. Available: https://doi.org/10.1016/b978-0-12-821082-6.00020-0

[12] F. Valente, A. Scarano, G. Murmura, G. Varvara, B. Sinjari, F. Mandelli, M. Piattelli, S. Caputi, and T. Traini, "Collagen fibres orientation in the bone matrix around dental implants: Does the implant's thread design play a role?" *International Journal of Molecular Sciences*, vol. 22, no. 15, p. 7860, Jul. 2021. [Online]. Available: https://doi.org/10.3390/ijms22157860

[13] H. Frost, "Defining osteopenias and osteoporoses: Another view (with insights from a new paradigm)," *Bone*, vol. 20, no. 5, pp. 385–391, 1997. [Online]. Available: https://www.sciencedirect.com/science/article/pii/S8756328297000197

[14] J. D. BOBYN, A. H. GLASSMAN, H. GOTO, J. J. KRYGIER, J. E. MILLER, and C. E. BROOKS, "The effect of stem stiffness on femoral bone resorption after canine porous-coated total hip arthroplasty," *Clinical Orthopaedics and Related Research*, vol. 261, pp. 196–213, Dec. 1990. [Online]. Available: https://doi.org/10.1097/00003086-199012000-00022

[15] A. Palmquist, A. Snis, L. Emanuelsson, M. Browne, and P. Thomsen, "Long-term biocompatibility and osseointegration of electron beam melted, free-form–fabricated solid and porous titanium alloy: Experimental studies in sheep," *Journal of Biomaterials Applications*, vol. 27, no. 8, pp. 1003–1016, May 2013. [Online]. Available: https://doi.org/10.1177/0731684411431857

[16] T. G. Bromage, H. M. Goldman, S. C. McFarlin, J. Warshaw, A. Boyde, and C. M. Riggs, "Circularly polarized light standards for investigations of collagen fiber orientation in bone," *The Anatomical Record Part B: The New Anatomist*, vol. 274B, no. 1, pp. 157–168, 2003. [Online]. Available: https://anatomypubs.onlinelibrary.wiley.com/doi/abs/10.1002/ar.b.10031

[17] A. Ascenzi and E. Bonucci, "A QUANTITATIVE INVESTIGATION OF THE BIREFRINGENCE OF THE OSTEON," *Cells Tissues Organs*, vol. 44, no. 3, pp. 236–262, 1961. [Online]. Available: https://doi.org/10.1159/000141725

[18] R. M. A. Azzam, "Stokes-vector and mueller-matrix polarimetry [invited]," *Journal of the Optical Society of America A*, vol. 33, no. 7, p. 1396, Jun. 2016. [Online]. Available: https://doi.org/10.1364/josaa.33.001396

[19] L. Y. Lung, C. Po-chun, Y. Tsung-chih, L. J. Fung, and Y. Tsung-tse, "Using polarimeter and stokes parameters for measuring linear birefringence and diattenuation properties of optical samples," *EPJ Web of Conferences*, vol. 6, p. 32001, 2010. [Online]. Available: https://doi.org/10.1051/epjconf/20100632001

[20] J. Freudenthal, A. Leadbetter, J. Wolf, B. Wang, and S. Segal, "A photoelastic modulator-based birefringence imaging microscope for measuring biological specimens," in *SPIE Proceedings*, Q. Luo, X. Li, Y. Gu, and Y. Tang, Eds. SPIE, Nov. 2014. [Online]. Available: https://doi.org/10.1117/12.2071271

[21] D. G. Lowe, "Distinctive image features from scale-invariant keypoints,"

International Journal of Computer Vision, vol. 60, no. 2, pp. 91–110, Nov. 2004. [Online]. Available: https://doi.org/10.1023/b:visi.0000029664.99615.94

[22] M. A. Fischler and R. C. Bolles, "Random sample consensus," *Communications of the ACM*, vol. 24, no. 6, pp. 381–395, Jun. 1981. [Online]. Available: https://doi.org/10.1145/358669.358692

[23] P. Fratzl, O. Paris, K. Klaushofer, and W. J. Landis, "Bone mineralization in an osteogenesis imperfecta mouse model studied by small-angle x-ray scattering." *Journal of Clinical Investigation*, vol. 97, no. 2, pp. 396–402, Jan. 1996. [Online]. Available: https://doi.org/10.1172/jci118428

[24] H. Singh, "The saxs guide–getting acquainted with the principles," 2013.

[25] M. Liebi, M. Georgiadis, J. Kohlbrecher, M. Holler, J. Raabe, I. Usov, A. Menzel, P. Schneider, O. Bunk, and M. Guizar-Sicairos, "Small-angle x-ray scattering tensor tomography: model of the three-dimensional reciprocal-space map, reconstruction algorithm and angular sampling requirements," *Acta Crystallographica Section A Foundations and Advances*, vol. 74, no. 1, pp. 12–24, Jan. 2018. [Online]. Available: https://doi.org/10.1107/s205327331701614x

[26] L. C. Nielsen, P. Erhart, M. Guizar-Sicairos, and M. Liebi, "Improved small-angle x-ray scattering tensor tomography with unrestricted spherical harmonics," 2022, *In preparation.*

[27] *MATLAB version 9.12.0.1884302 (R2022a)*, The Mathworks, Inc., Natick, Massachusetts, 2022.

[28] A. Vedaldi and B. Fulkerson, "VLFeat: An open and portable library of computer vision algorithms," 2008. [Online]. Available: http://www.vlfeat.org/

[29] O. Bunk, M. Bech, T. H. Jensen, R. Feidenhans'l, T. Binderup, A. Menzel, and F. Pfeiffer, "Multimodal x-ray scatter imaging," *New Journal of Physics*, vol. 11, no. 12, p. 123016, Dec. 2009. [Online]. Available: https://doi.org/10.1088/1367-2630/11/12/123016

[30] M. Georgiadis, A. Schroeter, Z. Gao, M. Guizar-Sicairos, M. Liebi, C. Leuze, J. A. McNab, A. Balolia, J. Veraart, B. Ades-Aron, S. Kim, T. Shepherd, C. H. Lee, P. Walczak, S. Chodankar, P. DiGiacomo, G. David, M. Augath, V. Zerbi, S. Sommer, I. Rajkovic, T. Weiss, O. Bunk, L. Yang, J. Zhang, D. S. Novikov, M. Zeineh, E. Fieremans, and M. Rudin, "Nanostructure-specific x-ray tomography reveals myelin levels, integrity and axon orientations in mouse and human nervous tissue," *Nature Communications*, vol. 12, no. 1, May 2021. [Online]. Available: https://doi.org/10.1038/s41467-021-22719-7

[31] M. Mello and B. Vidal, "Anisotropic properties of toluidine blue stained collagen," *Annales d'histochimie*, vol. 18, pp. 103–22, 04 1973.

[32] S. Viguet-Carrin, P. Garnero, and P. D. Delmas, "The role of collagen in bone strength," *Osteoporosis International*, vol. 17, no. 3, pp. 319–336, Dec. 2005. [Online]. Available: https://doi.org/10.1007/s00198-005-2035-9

[33] M. D. Vlad, E. F. Aguado, S. G. González, I. C. Ivanov, E. V. Şindilar, I. Poeată, A. Ş. Iencean, M. Butnaru, E. R. Avădănei, and J. L. López, "Novel titanium-apatite hybrid scaffolds with spongy bone-like micro architecture intended for spinal application: In vitro and in vivo study," *Materials Science and Engineering: C*, vol. 110, p. 110658, May 2020. [Online]. Available: https://doi.org/10.1016/j.msec.2020.110658

[34] J. D. BOBYN, R. M. PILLIAR, and G. C. CAMERON, H. U.and WEATHERLY, "The optimum pore size for the fixation of porous-surfaced metal implants by the ingrowth of bone," *Clinical Orthopaedics and Related Research®*, vol. 150, 1980. [Online]. Available: https://journals.lww.com/clinorthop/Fulltext/1980/07000/The_Optimum_Pore_Size_for_the_Fixation_of.45.aspx

A

Appendix

A.1 Sample Overview

Solid Ti6Al4V

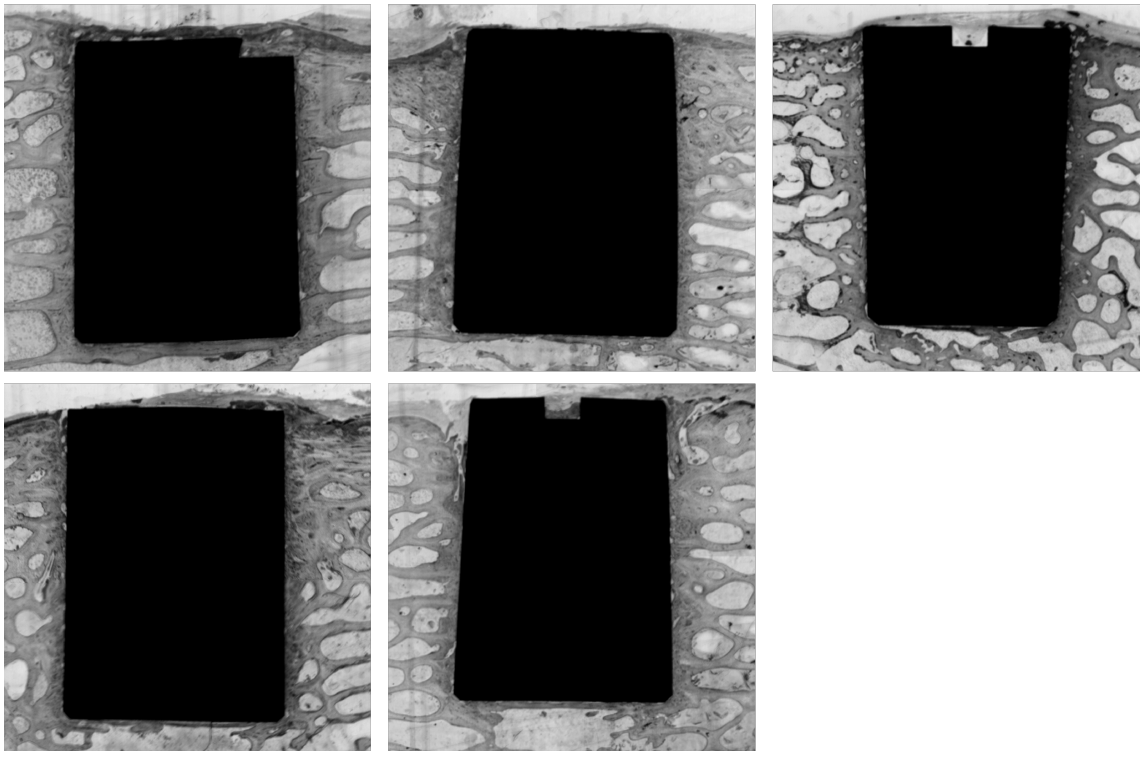

Porous Ti6Al4V with large struts

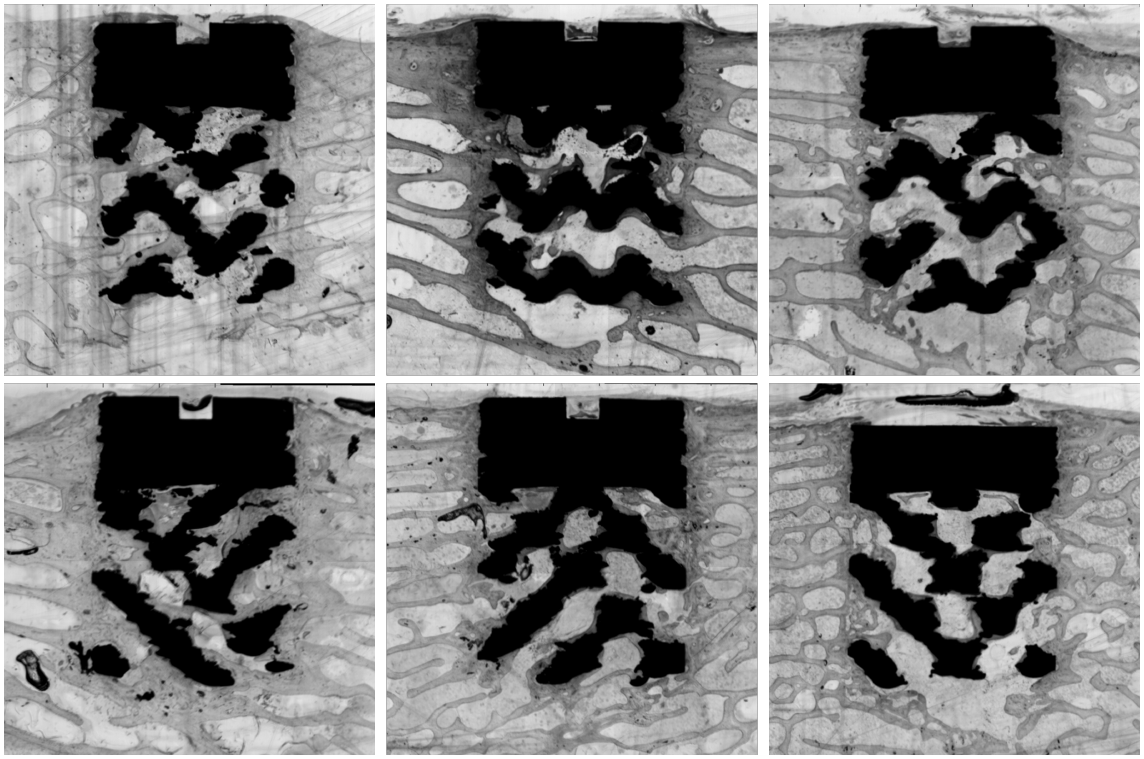

Porous Ti6Al4V with small struts

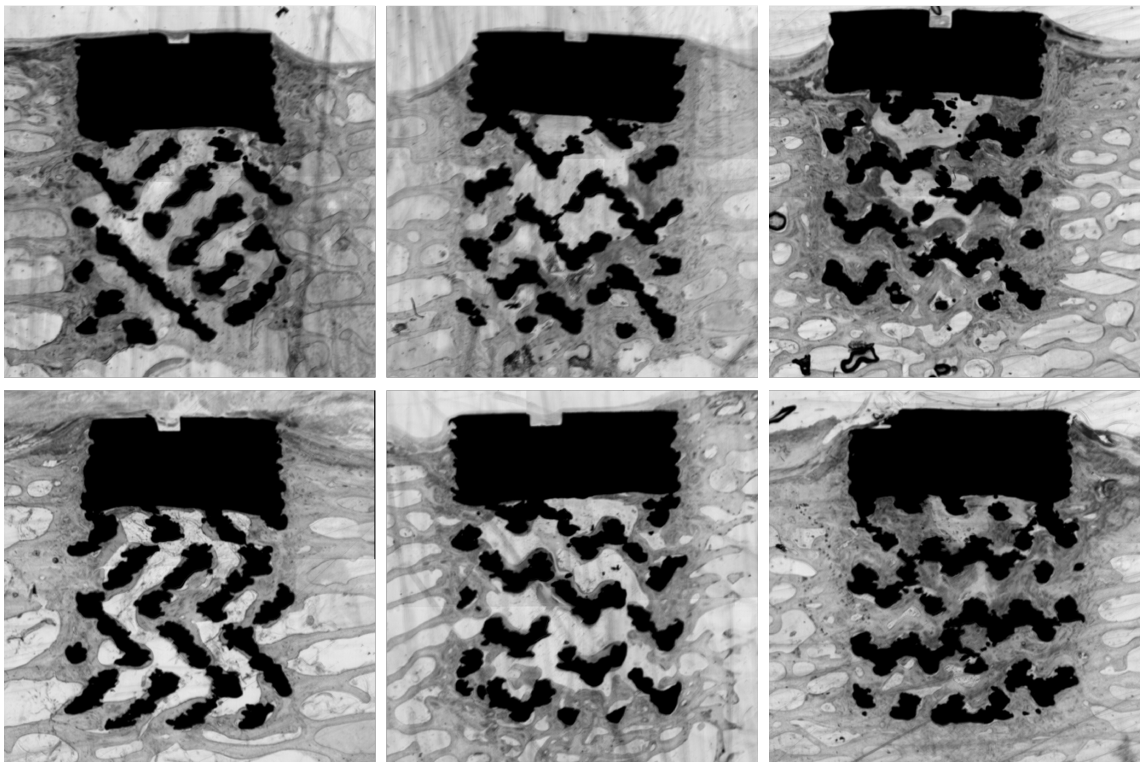

Porous CoCr with small struts

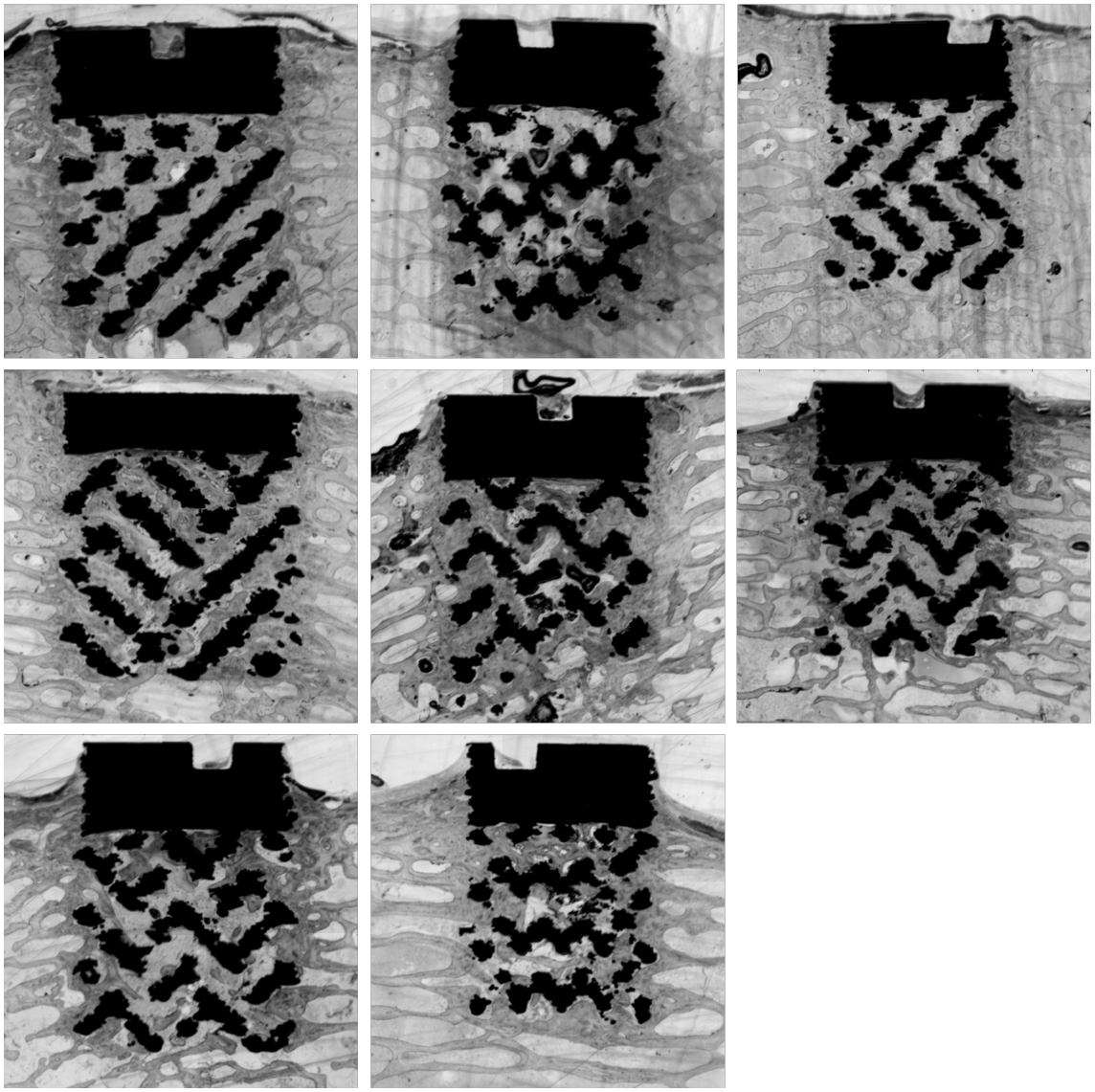

A.2 Microscope technical details

Light source:		LED
Wavelengths:		475, 535, 615, 655 nm
Image size:		2048 × 2048 pixels
Field of view:		
	2x	5.69 mm square
	10x	1.14 mm square
	20x	0.56 mm square
Pixel size:		
	2x	2.78 µm
	10x	0.56 µm
	20x	0.27 µm
Resolution:		
	2x	5 µm
	10x	2 µm
	20x	1 µm
Fast axis angle		
	Range:	$-90° \rightarrow 90°$ degrees
	Resolution:	0.5°

A.3 Angle of fast axis in metallic implants

	Inside (°)		Outside (°)
Large struts (Ti6Al4V)	-39	35	14
	-28	57	-17
	-29	-7	-13
	(-)	23	(-)
	(-)	-7	0
	-38	18	-10
Small struts (CoCr)	-46	32	-6
	-32	44	-3
	-34	40	-19
	-40	38	-6
	-35	18	-14
	-33	40	-15
	-42	32	-7
	-35	1	-10
Small struts (Ti6Al4V)	-51	44	11
	-30	46	-5
	-41	46	-3
	-25	23	12
	2	46	-5
	-23	44	22
	-41	44	-13

DEPARTMENT OF PHYSICS
CHALMERS UNIVERSITY OF TECHNOLOGY
Gothenburg, Sweden
www.chalmers.se

CHALMERS
UNIVERSITY OF TECHNOLOGY